Eruptive chronology of Tungurahua volcano (Ecuador) revisited based on new K-Ar ages and geomorphological reconstructions

Mathilde Bablon, Xavier Quidelleur, Pablo Samaniego, Jean-Luc Le Pennec, Pierre Lahitte, Céline C. Liorzou, Jorge Eduardo Bustillos, Silvana Hidalgo

Eruptive chronology of Tungurahua volcano (Ecuador) revisited based on new K-Ar ages and geomorphological reconstructions

Mathilde Bablon [a*], Xavier Quidelleur [a], Pablo Samaniego [b], Jean-Luc Le Pennec [b,c], Pierre Lahitte [a], Céline Liorzou [d], Jorge Eduardo Bustillos [e], Silvana Hidalgo [c]

[a] GEOPS, Univ. Paris-Sud, CNRS, Université Paris-Saclay, 91405 Orsay, France

[b] Laboratoire Magmas et Volcans, Université Clermont Auvergne, CNRS, IRD, OPGC, F-63000 Clermont-Ferrand, France

[c] Instituto Geofísico, Escuela Politécnica Nacional, Ap. 17-01-2759, Quito, Ecuador

[d] Université de Bretagne Occidentale, Domaines Océaniques IUEM, 29280 Plouzané, France

[e] Facultad de Geología, Universidad Central del Ecuador, Casilla 872 A, Quito, Ecuador

Corresponding author: mathilde.bablon@u-psud.fr (M. Bablon).

ABSTRACT

This study focuses on the evolution through time of Tungurahua volcano (Ecuador), and provides new information regarding its history. Eighteen new K-Ar ages constrain its construction and the activity of its three successive edifices. We show that the volcano is much younger than expected. Indeed, the older edifice activity only began around 293 ± 10 ka, and ended at 79 ± 3 ka. After ~50 ka of quiescence, the second edifice started growing at 29 ± 2 ka after a major sector collapse, and itself collapsed at ~3 ka. Since then, the third edifice filled the amphitheatre and is still active. Together with numerical reconstructions of the morphology of the three edifices flanks before erosion, these new ages allow us to quantify the magmatic productivity rates during their construction, from 0.6 ± 0.3 and 0.9 ± 0.2 km^3/ka for the two older edifices to 2.5 ± 1.0 km^3/ka for the youngest, as well as an

erosion rate of 0.2 ± 0.1 km^3/ka, occurring since the end of Tungurahua I construction. Major and trace element contents of lavas from the three edifices display rather similar trends. Combined with our new ages, the magmatic signature through time does not seem to have been significantly affected either by the sector collapses experienced by the volcano, or by changes of the deep magmatic source. Finally, our results show that the K-Ar dating method by the unspiked Cassignol-Gillot technique performed on groundmass can be successfully applied to lava flows older than the Holocene, while the uncertainties related to younger units can prevent an accurate age determination. Particularly, this method can be applied to Quaternary volcanoes from the Ecuadorian arc, with many of them remaining without knowledge of the timing of their past activity.

Keywords:
Ecuador
Tungurahua volcano
K-Ar dating
Geomorphology
Geochemistry

1. Introduction

The Ecuadorian arc presents a remarkably dense volcanism, composed of about 85 Quaternary volcanic edifices (Hall et al., 2008; Bernard and Andrade, 2011). Twenty-five of them are potentially active or presently erupting, such as Sangay, Cotopaxi, Reventador and Tungurahua volcanoes (Fig. 1; Bernard and Andrade, 2011). Tungurahua volcano (5023 m a.s.l.; Lat. 01°28'S; Long. 78°27'W) is one of the most active volcanoes in the Andean Northern Volcanic Zone with at least one eruption per century since the 13th century (Le Pennec et al., 2008, 2016). It is characterized by a strombolian to subplinian activity, and

experienced at least two major sector collapses during the last 30 ka (Hall et al., 1999; Le Pennec et al., 2013). Since 1999, the ongoing eruption has seriously threatened surrounding villages and infrastructures (Samaniego et al., 2008; Le Pennec et al., 2012). The recent activity is well studied and carefully monitored (e.g., Molina et al., 2005; Arellano et al., 2008; Kumagai et al., 2011; Hall et al., 2013; Bernard et al., 2014; Hidalgo et al., 2015), but the timing of its pre-Holocene history remains poorly documented. Reconstructing the past eruptive history of Tungurahua volcano is essential to better understand its growth and evolution. This study combines stratigraphic analyses, new K-Ar ages and geomorphometric reconstructions to better constrain the construction and destruction stages of Tungurahua volcano through time, and to quantify its magmatic output rates, as well as the erosion rate occurring during quiescence periods. In addition, geochemical analyses allow us to study the long-term evolution of the lavas composition. We show in particular that the initial activity of Tungurahua volcano is much younger than previously thought, and that its construction is characterized by an increase of the eruptive rate since the last 3 ka BP.

2. Geological context

The Andean volcanic arc originates from the subduction of the oceanic Nazca plate beneath the continental South American plate. The arc comprises four distinct zones, including the Northern Volcanic Zone (NVZ), which lies in Ecuador and Colombia. To the west of the NVZ, an oceanic plateau, the Carnegie ridge, subducts below Ecuador (Fig. 1a). It has been proposed that the subduction of this ridge may impact the thermal gradient at depth and the deep magmatic sources (e.g., Samaniego et al., 2002; Bourdon et al., 2003; Hidalgo et al., 2012; Ancellin et al., 2017), which could explain the high density of volcanoes observed in Ecuador (Martin et al., 2014). Tungurahua volcano is located in the southern part of the Ecuadorian volcanic arc, on the Eastern Cordillera (Fig. 1b). Constructed upon the

77 Palaeozoic-Mesozoic metamorphic basement (Aspden and Litherland, 1992), this andesitic
78 stratovolcano is surrounded by the Puela (S), Chambo (W) and Pastaza (N) rivers (Fig. 2).
79 The upper part of the edifice presents steep flanks with 40° slopes, while ~20-25° slope
80 plateaux incised by deep valleys constitute its lower part, with a progressive change in
81 steepness. The morphology of the eastern flank shows features of glacial erosion (u-shaped
82 valleys; Clapperton, 1990; Heine, 2000), as well as deep fluvial incisions due to the tropical
83 precipitation regime. It contrasts with the western flank which is smoothed by the recent
84 volcanic deposits. The internal structure and plumbing system of Tungurahua volcano are not
85 well known. Nevertheless, petrological, melt inclusions, seismic tomography and
86 interferometric studies suggest the presence of a subvertical upper conduit located above a
87 shallow magmatic reservoir, supplied by mafic magmas from a deeper reservoir, located
88 around 5 and 8.5 km below the summit, respectively (Molina et al., 2005; Samaniego et al.,
89 2011; Kumagai et al., 2011; Champenois et al., 2014; Myers et al., 2014).
90 Previous works showed that Tungurahua volcano was built in three construction stages,
91 namely Tungurahua I, II and III, and experienced two major sector collapse events (Hall et al.,
92 1999; Le Pennec et al., 2013, 2016). Inclined plateaux of the northern, eastern and southern
93 flanks essentially belong to Tungurahua I activity, which started during the Pleistocene, based
94 on two available whole-rock K-Ar ages of 770 ± 5 and 350 ± 4 ka (Barberi et al., 1988). The
95 western part of Tungurahua I was destroyed by a first sector collapse, ^{14}C dated at
96 33.1 ± 0.2 ka BP (Le Pennec et al., 2013), which might have been triggered by a silicic
97 cryptodome intrusion (Le Pennec et al., 2006). The resulting amphitheatre volume was
98 estimated at 10 km^3 (Bustillos, 2008), but the collapse scar location is not accurately
99 identified in the present-day edifice morphology. Tungurahua II lavas and deposits then filled
100 the amphitheatre, before being destroyed in turn by a new western sector collapse ^{14}C dated at
101 2955 ± 90 BP (Hall et al., 1999) and 2960 ± 30 BP (Le Pennec et al., 2013). It was triggered

by a new viscous intrusion or magma mixing occurring in the chamber (Hall et al., 1999; Le Pennec et al., 2006, 2013). The avalanche deposits associated with this second event cover between 23 and 80 km², for a collapse volume estimated between 2.8 and 6 km^3 (Bustillos, 2008 and Hall et al., 1999 respectively). However, the area and the volume obtained by Hall et al. (1999) are necessarily higher because they mapped as a single sector collapse the deposits of the two sector collapses of Tungurahua, and the one experienced by Huisla volcano (Fig. 2; Bustillos, 2008). The southern location of the scar boundary is well delimited in the morphology, whereas the northern part was first proposed along the Pondoa plateau (Hall et al., 1999), and recently shifted to the west based on geomorphological and seismological studies (Molina et al., 2005; Le Pennec et al., 2006; Fig. 2). Due to this collapse and continuous erosion, remnants of Tungurahua II mainly crop out on the eastern summit area and in the southwestern valleys (i.e. the Tiacos lava sequences of Hall et al., 1999). Products from the younger and still active Tungurahua III cone have then filled the amphitheatre left by the second sector collapse (Hall et al., 1999; Le Pennec et al., 2006, 2013). Lavas and pyroclastic flow deposits, as well as tephra fall and epiclastic layers displaying basaltic andesite to dacitic composition make up the present western flank. Eight pre-Columbian eruptive periods were identified, and five major eruptions occurred during historical times: AD 1640-1641, 1773-1776, 1886-1888, 1916-1918 and 1999-present, with therefore a recurrence rate of about one pyroclastic flow-forming event per century (Hall et al., 1999; Le Pennec et al., 2008, 2016).

Given that Tungurahua III activity has already been well described and ^{14}C dated (Hall et al., 1999; Le Pennec et al., 2006, 2008, 2013, 2016), in this study we focus on the two older edifices, Tungurahua I and II.

3. Materials and methods

127 *3.1. Sampling*

128 Twenty-four fresh hand-size samples of lava flows were collected during several field
129 trips from 2013 to 2016 (Fig. 3a). Geographical coordinates of the samples are provided in
130 Table 1 and the associated KMZ file is available in Appendix C. In order to constrain the
131 onset of the volcano activity, seven samples were taken from the basal flows, close to the
132 contact with the metamorphic basement (PS-102, PS-106, PS-110, 16EQ15, 16EQ12, PS-118
133 and 16EQ26). Sample 16EQ12 was collected from a breccia containing monogenic blocks.
134 Seven lavas were sampled in the uppermost part of Pondoa, Runtún, Ulba and Patacocha
135 plateaux (Fig. 2). Because of their position in the stratigraphic sequence of these plateaux, we
136 infer that they were emplaced late in Tungurahua I history (PS-116, PS-99, 16EQ16, 16EQ17,
137 16EQ25, TUNG 3, TUNG4). Seven lavas of Tungurahua II were sampled along Ulba valley
138 (PS-111, 16EQ19), in Las Juntas and Juive Grande areas (PS-107, PS-109), and near
139 Palitahua waterfalls (Fig. 2; PS-117, PS-119, 16EQ13). Two recent lavas were also sampled
140 to compare our dating method with published ^{14}C ages: a dacitic flow near Cusúa (16EQ36),
141 which belongs to the beginning of Tungurahua III activity (Hall et al., 1999), and the Baños
142 lava flow (16EQ37). In addition, a massive lava flow erupted from an unknown source and
143 exposed between the Pastaza valley and Vizcaya village was also sampled (16EQ20). The aim
144 was to determine whether it could be contemporaneous with Tungurahua volcano activity.
145
146 *3.2. K-Ar dating*

147 The potassium-argon (K-Ar) dating method was applied here by using the unspiked
148 Cassignol-Gillot technique (Cassignol and Gillot, 1982), which was developed for Quaternary
149 volcanics with low radiogenic argon ($^{40}Ar^{*}$) contents (Gillot et al., 2006). It has been shown to
150 be especially suitable for dating young subduction lavas with low K and high Ca contents, as
151 is the case for instance in South America and in the Lesser Antilles (e.g., Samper et al., 2009;

Germa et al., 2011). The technique relies on the detection of a very small difference between the isotopic $^{40}Ar/^{36}Ar$ ratio extracted from the sample and the atmospheric ratio. The radiogenic argon content, which derived from the radioactive decay of ^{40}K, together with the potassium content of the sample and the ^{40}K decay constant (Steiger and Jäger, 1977), allow determining the age of the lava sample.

3.2.1. Sample preparation

The groundmass is the last phase to crystallize when lavas cool. It is thus enriched in incompatible elements, including potassium, and in equilibrium with the atmosphere. Hence the initial argon isotopic ratios in the groundmass are atmospheric, and it is devoid of radiogenic argon ($^{40}Ar^{*}$). On the other hand, phenocrysts can carry inherited $^{40}Ar^{*}$, that might bias ages significantly (e.g., Harford et al., 2002; Samper et al., 2008). We therefore carried out our measurements on the groundmass following a careful mineralogical separation. Observation of thin sections (available on Appendix A) helped us to attest of the samples freshness, and to determine the size fraction. The selected samples were crushed and sieved at 80-125 µm, 80-160 µm, or 125-250 µm, then ultrasonically washed with a 10% nitric acid solution and deionized water. Heavy liquids, mainly bromoform, were used to isolate the groundmass by removing heavy mafic minerals, and light weathered fractions, if present. Finally, the separation was refined with a magnetic separator, which removed non-magnetic plagioclases remaining within the magnetic groundmass, as their respective ranges of density overlap. The obtained fractions of groundmass, which amount to only a few percent of the initial sample, have a narrow density range, with a typical value of 2.71. Their homogeneity was checked under a binocular magnifier, and both potassium and argon measurements were carried out at the Laboratoire GEOPS of Université Paris-Sud (Orsay, France).

177 *3.2.2. Potassium and argon measurements*

178 Potassium was measured with an Agilent 240 Series AA flame absorption spectrometer,
179 after dissolving samples with an acid attack. Results were corrected with reference values of
180 MDO-G (K = 3.510%; Gillot et al., 1992) and BCR-2 (K = 1.481%; Raczek et al., 2001)
181 standards.

182 Argon was measured using a mass spectrometer similar to the one described by Gillot
183 and Cornette (1986). Very stable conditions reached during the measurements rendered the
184 use of the ^{38}Ar spike, needed for the conventional K-Ar technique, unnecessary. Gases
185 extracted by fusing the sample were purified with high temperature Ti foam and SAES
186 getters. An air pipette containing a known amount of ^{40}Ar atoms was used to calibrate the
187 mass spectrometer. Another air pipette, with the same ^{40}Ar signal as the sample to be dated,
188 allows an accurate atmospheric correction to be performed.

189 The accuracy of this correction and of the ^{40}Ar calibration are routinely checked by
190 analyses of international standards samples measurements, such as ISH-G (1301-1302 AD;
191 Gillot et al., 1992) and HD-B1 (24.21 ± 0.32 Ma; Hess and Lippolt, 1994).

192 The total relative age uncertainty (σ_{tot}) is calculated using the following formula:

193 $$\sigma_{tot} = \sqrt{\sigma_K^2 + \sigma_{^{40}Ar_{cal}}^2 + \sigma_{^{40}Ar^*}^2}$$

194 The relative uncertainties of the potassium content (σ_K) and the ^{40}Ar calibration ($\sigma_{^{40}Ar_{cal}}$) are
195 both evaluated at 1%. The uncertainty of radiogenic argon ($\sigma_{^{40}Ar^*}$) depends on the radiogenic
196 content of the sample. For young samples, this uncertainty is larger because of their high
197 atmospheric and low radiogenic argon contents. The ^{40}Ar* detection limit of our
198 measurements is presently at 0.1% (Quidelleur et al., 2001).

199 All potassium and argon measurements were performed at least twice in order to check
200 their reproducibility within uncertainty. Final ages and uncertainties were calculated by

averaging each analysis, weighted by their $^{40}Ar^*$ content. However, for the youngest samples where $^{40}Ar^*$ content is lower than 0.1%, ages were calculated using an unweighted average. Ages obtained here are given at the 1 σ confidence level (Table 1).

3.3. Geochemical analyses

Major and trace element whole-rock contents of all samples were measured at the Laboratoire Géosciences Océan of the Université de Bretagne Occidentale (Brest, France). Agate-crushed powders of the twenty-four samples were analysed by ICP-AES (Inductively Coupled Plasma - Atomic Emission Spectrometry), following the analytical procedure detailed in Cotten et al. (1995). Relative uncertainties are ≤ 2% for major elements and ≤ 5% for trace elements. Major elements data were recalculated to a total of 100% on a water free-basis and together with trace elements are provided in Table 2. Our geochemical database was completed by seventy-two unpublished major and trace elements analyses of samples from the three edifices and blocks from the sector collapse deposits (Hall et al., 1999; Bustillos, 2008), which are presented in Appendix B.

3.4. Numerical reconstructions of past morphology

Numerical reconstructions of palaeotopographies were used to model the morphology of the volcano during its main phases of construction, erosion and collapse. They provided information regarding evolution of the magmatic productivity through time, and the erosion rates, which are influenced by precipitation and glacial-interglacial alternating periods. The present topographic data are extracted from a 30-m SRTM Digital Elevation Model (DEM). The reconstruction method used here was developed in Lahitte et al. (2012) and improved in Germa et al. (2015). It is summarized below.

225 Past Tungurahua topographic models are constrained from points selected from the
226 present-day topography, as belonging to non-eroded surfaces. In general, they are from crests,
227 upper parts of plateaux, planeze surfaces or recent deposits (Fig. 4a and b). ShapeVolc, a
228 specifically developed method, is used for modelling the different palaeotopographies based
229 on these points (Lahitte et al., 2012). This method first finds a global model, by defining the
230 best summit location and the parameters of the function that define a revolution surface,
231 which best fit the selected points following a least-squares method adjustment. Thereby,
232 Tungurahua I reconstruction displays a conical shape with linear flank profiles and an
233 elliptical base, while Tungurahua II and III have an exponential shape with a concave profile
234 (Fig. 4c). The software then adjusts the first-order modelling by modifying locally the
235 parameters of the global function, in order to take into account local elevation variations, i.e.
236 the irregularity of the surface of each stage of construction (Lavigne et al., 2013; Germa et al.,
237 2015). These second-order surfaces correspond to our final construction models. The
238 evolution of Tungurahua I altitude after its erosion is calculated by lowering each elevation of
239 the model as a linear function of time, between the model elevation and the present
240 topography. Moreover, as the geometry of the depressions of the collapses is not precisely
241 known, we modelled them by an interpolation between points currently located on the edge of
242 the scars and two profiles forming the possible bottom surface represented by the
243 discontinuous curves in Fig. 4a, located so as to respect the collapse volumes estimates,
244 respectively of ~10 and ~2.8 km^3, based on the deposits located in the Río Chambo valley
245 (Hall et al., 1999; Bustillos, 2008).

246 Finally, the reconstruction of pre-Tungurahua topography is obtained by selecting DEM
247 points which belong to the metamorphic basement outcropping around the volcano, in order
248 to extrapolate them under the present volcano surface. This palaeosurface is modelled
249 applying a Local Polynomial Interpolation method with a resolution of 100 m, using ArcGis

software. The model is therefore smooth, since we cannot constrain the exact morphology of the basement 300 ka ago, which is currently overlaid by Tungurahua products.

3.5. Magmatic productivity and erosion rates

The volume (V), either constructed (Vc) or eroded (Ve), corresponds to the integration of the difference between the upper and the lower surface, over the area of the edifice considered. In this fashion, the eroded volume is the difference between the modelled surface and the present topography (Δz). The deposits volume for each edifice corresponds to the difference between the surface elevation modelled at the end of their constructions and the one which preceded the edifice construction. Erosion that occurred during the Tungurahua I and II construction lowered the apparent volume of emitted magma. To take into account this erosion, we added to the raw volume the eroded volume estimated by considering that the erosion rate calculated for the last 80 ka was rather constant though time. The volume uncertainty (σ_V) is calculated using the following formula:

$$\sigma_V = V \,.\frac{\sigma_z}{\Delta z}$$

where the uncertainty of the elevation (σ_z) is defined as $\sigma_z = \sqrt{{\sigma_{i\,surf}}^2 + {\sigma_{f\,surf}}^2}$, where the uncertainties of the initial ($\sigma_{i\,surf}$) and the final ($\sigma_{f\,surf}$) surface elevation are estimated to 200 m for the interpolated surface before Tungurahua construction, 50 m for our surface models, and null for the present elevation. These uncertainties are obtained from the standard deviation of the elevation dispersion of the points selected to construct the palaeotopographies around the surface model, and calculated from the error map of the kriging interpolation method for the pre-Tungurahua surface (Ricci et al., 2015a).

Together with our new K-Ar ages, these volumes, divided by the period of activity or quiescence (ΔT), allow us to calculate the apparent magmatic productivity (MPR) and erosion (ER) rates of Tungurahua volcano, with $MPR = \frac{Vc}{\Delta T}$, and $ER = \frac{Ve}{\Delta T}$. As the parameters

involved in these ratios are independent, the uncertainty of the $\frac{\sigma_R}{R}$ ratio is then defined as the square root of the quadratic sum of the relative uncertainties of both stage duration (σ_T) and volume (σ_V). Consequently, the uncertainty of the magmatic productivity or erosion rate (σ_R) is calculated using the following formula:

$$\sigma_R = R \cdot \sqrt{\left(\frac{\sigma_V}{V}\right)^2 + \left(\frac{\sigma_T}{\Delta T}\right)^2}$$ where R is the considered rate.

The uncertainty on the duration is estimated from K-Ar ages uncertainty, which constrains the timing of each edifices construction and erosion. Consequently, because of the relatively good age precision, σ_R is mainly dominated by the volume uncertainty. Moreover, this technique of calculation based on numerical reconstructions is more accurate than traditional methods, which generally use approximate volumes. We also present the minimum and maximum values of emission rates, considering the upper and lower values of both volume and time period. However, we chose to only use the previous calculation method for discussion and comparisons, since it provides a more realistic result and takes into account the Gaussian distribution of the data. Results of the volumes, magmatic productivity and erosion rates calculations are provided in Table 3.

4. Results

4.1. Petrography of the samples

There is no clear mineralogy difference between the lava flows from the three edifices. Most of the Tungurahua lava flow samples have porphyric textures with a variable amount of plagioclase, orthopyroxene, clinopyroxene and olivine phenocrysts, except samples of Vizcaya lava flow (16EQ20) and the lower Runtún plateau (PS-110 and PS-106), which present a vitreous texture with scarce crystals (Appendix A). Sample PS-119, from the southern flank, also present some amphibole crystals, but none of our lava flow sample

299 contains biotite crystals. The groundmass contains plagioclase, pyroxene and Fe-Ti oxide
300 microcrysts separated by volcanic glass, and mainly represents about 50-70% of the rock
301 volume. Moreover, some samples present color variations of their groundmass, such as
302 16EQ15 and 16EQ17 from the Ulba plateau, 16EQ19 and PS-111 from the bottom of Ulba
303 Valley, PS-99 from the Runtún upper part, as well as PS-117 and PS-118 from the southern
304 flank (Fig. 3). These variations correspond to more or less differentiated magmas and display
305 that magma mixing processes occurred.
306

307 *4.2. K-Ar dating*

308 K-Ar ages obtained in this study are presented in Table 1 and Fig. 3 and 5. Six samples
309 were not considered because they were either altered (16EQ12) or too contaminated by
310 atmospheric argon (16EQ13, 16EQ19, 16EQ36, TUNG3) to yield a meaningful age.
311 Moreover, as the base and the top of Ulba sequence are well constrained by samples 16EQ15
312 and 16EQ17 respectively, dating sample 16EQ16 was not necessary, since it is an
313 intermediate lava located between the other two samples. Eighteen samples were successfully
314 dated, with the K content of the groundmass ranging between 1.122% and 3.253%, and the
315 maximum radiogenic argon content reaching 13.78%. These new data allow us to refine the
316 timing of activity of Tungurahua volcano. The oldest edifice is well constrained by eleven
317 ages, and was built between 293 ± 10 and 79 ± 3 ka. Our ages obtained for the lavas from
318 Ulba, Pondoa and Runtún plateaux range between 92 ± 1 and 79 ± 3 ka, and suggest a gap of
319 activity between 76 ka and the ~33 ka first sector collapse event (Fig. 5; Le Pennec et al.,
320 2013). The construction of Tungurahua II started at least 29 ± 2 ka (PS-117), therefore
321 quickly after the first sector collapse. Similarly than for Tungurahua I, we have no evidence of
322 activity between 27 and 15 ka. The five youngest ages are below 15 ka, but their relatively
323 large uncertainties prevent us to determine whether they belong to Tungurahua II, or are

younger than 3 ka and are part of Tungurahua III. Only lava from the sample PS-109 clearly belongs to Tungurahua II. We propose that samples PS-107, PS-111 and PS-119 are related to Tungurahua II activity, while the sample of Baños lava flow (17EQ37) was emitted in the early stage of Tungurahua III construction, based on their stratigraphic relationships, further described in the discussion. Finally, the Vizcaya lava flow (16EQ20) dated at 253 ± 5 ka, is coeval with the early construction of Tungurahua I.

4.3. Whole-rock geochemical analyses

The major and trace element contents for all samples are presented in Table 2. Loss on ignition (L.O.I) measurements are low, with a maximum value of 1.15%, which attests for samples freshness and their low content in volatiles.

4.3.1. Major elements

Tungurahua lava flows show typical trends of subduction-related volcanic rocks, and are similar to the previous analyses from its different units and the published data from the Eastern Cordillera (Fig. 6). Indeed, most samples fall within basaltic andesite and andesite fields in the K_2O vs. SiO_2 diagram (Peccerillo and Taylor, 1976; Fig. 6), and two samples are dacites (16EQ17 and 16EQ20). Silica content ranges between 53.3 and 67.0 wt.%, and K_2O content between 1.3 and 3.6 wt.%. Consequently, rocks from Tungurahua belong to the medium-K calc-alkaline series, except for some samples from Tungurahua I, which are more alkaline-rich and belong to the high-K calc-alkaline series.

Variation diagrams, shown as a function of Th (as a differentiation index), also show typical trends of subduction zone volcanism (Fig. 7). Th is a highly incompatible element, which is not fractionated during partial melting or fractional crystallization process. The decrease of MgO, Fe_2O_3, Al_2O_3, CaO and TiO_2 (Fig. 7a, b, c and d) suggests fractional

crystallization of plagioclase and Fe-Ti oxide phenocrysts present in the samples, sometimes along with pyroxene and olivine crystals (Appendix A). Magmas are not evolved enough to loose K_2O and Na_2O through incorporation into crystals, and hence the alkali content increases as the fractional crystallization proceeds (Fig. 7e and f).

4.3.2. Trace elements

Spider diagrams of trace elements, normalized to the primitive mantle (Sun and McDonough, 1989; Fig. 8a), shows enrichment of Large-Ion Lithophile Elements (LILE; Rb, Ba, and K) and depletion of High-Field Strength Elements (HFSE; Nb, Ti and Y), also typical of subduction magmas. These signatures are also found on the Rare Earth Elements (REE) diagram normalized to chondrites values (Sun and McDonough, 1989; Fig. 8b), with an enrichment in Light REE (LREE; to the left) compared to Heavy REE (HREE, to the right), without a negative Eu anomaly.

Overall, lavas from Tungurahua I have higher REE contents, which can be linked with its high-K signature (Fig. 6). In the Sr/Y versus Y diagram (Fig. 9e), most of the rocks plot in the classical calc-alkaline arc lavas field, but some lavas are more depleted in Y and tend toward an "adakitic" signature. However, all samples are too enriched in Yb and too depleted in La to reach the "adakitic" domain in the La/Yb versus Yb diagram (Fig. 9f). Moreover, the Sr/Y ratio decreases as the fractional crystallization proceeds, whereas La/Yb and Th are positively correlated (Fig. 9c and d, respectively). Tungurahua I lavas are rather scattered, particularly for Pondoa basal unit and younger plateau lavas, which differ significantly from the general trend (Fig. 7). Indeed, old lavas of Pondoa, including PS-102, show a high enrichment in all incompatible elements and REE, notably Y and Yb (Fig. 8; Fig. 9e and f). Overall, all samples are porphyritic except one from the upper part of Ulba plateau (16EQ17), which is almost entirely crystallized and presents a trachytic texture (Appendix A). It is the

most evolved sample of plateau lavas, and presents high enrichment in the most incompatible elements and REE (Fig. 7; Fig. 8; Fig. 9).

Tungurahua II and III lavas compositions are rather homogeneous, and major and trace element contents do not allow us to clearly discriminate between these two different edifices. However, it can be noticed that sample PS-117, which corresponds to the beginning of Tungurahua II activity shortly after the first sector collapse event, is the most depleted in HFSE and HREE, notably in Nb, Y and Yb (Fig. 8; Fig. 9e and f). Moreover, the composition of the "Cusúa dacite" sample (16EQ36) is slightly less differentiated than the one of Hall et al. (1999), with 62.2 wt.% of SiO_2. Finally, the Vizcaya lava flow (16EQ20) differs significantly from Tungurahua lavas for most major elements (Fig. 6; Fig. 7) and for some trace elements (Fig. 9b).

4.4. Geomorphological reconstructions

Palaeotopographical reconstructions were used to propose a temporal evolution of Tungurahua volcano morphology (Fig. 10; Table 3).

The morphology of the metamorphic basement suggests that a north-south crest was present under the present edifice before its construction (Fig. 10a), extending the one currently found south of the volcano. As the volcano grew, Río Chambo and Pastaza palaeovalleys (Fig. 2), which were present initially, were shifted westward and northward.

Overall, the present Tungurahua edifice presents a conic morphology, with a rather circular base and a concave profile. According to our extrapolation of the basement and the present topography, the present volume of this volcano is 108 ± 30 km^3 (Table 3), with a basal surface of about 150 km^2. Given our maximum age of 293 ± 10 ka, the apparent production rate is 0.4 ± 0.1 km^3/ka.

In detail, Tungurahua I was a volcano with a rather flat summit, which peaked at a minimum elevation of 4500 m (Fig. 10b), 2 km southeast to the present summit. Based on our numerical reconstructions, the volume of Tungurahua I at the end of its construction was 56 ± 33 km^3. Considering that the erosion rate affecting its flanks during its growth was similar to the erosion rate calculated since the end of its construction, we obtain an eroded volume of 68 ± 41 km^3 between ~293 and 81 ka. This volume is added to the first volume of 56 ± 33 km^3, which provides a total volume of 124 ± 74 km^3 of products emitted during the ~212 ka of Tungurahua I construction (Table 3). As a result, the magmatic productivity rate of this first edifice was 0.6 ± 0.3 km^3/ka. A quiescence period favoured the erosion of Tungurahua I flanks between 80 and 33 ka (Fig. 10c). Then, the sudden loss of ~10 km^3 of deposits (Bustillos, 2008) during the first western sector collapse at ~ 33 ka (Fig. 10d; Table 3) may have favoured the rise of magma (e.g., Hildenbrand et al., 2004) and the rapid construction of Tungurahua II within the resulting amphitheatre (Fig. 10e). This second edifice culminated at about 5070 m, with a concave upward profile similar to the present volcano. Although the volume of the emitted products (24 ± 4 km^3) is significantly lower than the one calculated for the first edifice, its eruptive rate was similar (0.9 ± 0.2 km^3/ka) given the shorter duration of this stage, between 29 ± 2 ka (Table 1) and 2.96 ± 0.03 ka (Le Pennec et al., 2013). A new flank failure occurred at ~3 ka (Fig. 10f), mobilizing around 3 km^3 of deposits (Bustillos, 2008) from the western summit part. Finally, the third and still active edifice was rapidly constructed in the depression left by this collapse (Fig. 10g). Tungurahua III is characterized by the lowest volume of deposits (7 ± 3 km^3), but displays a relatively high eruptive rate of 2.5 ± 1.0 km^3/ka. In addition, an erosion rate of 0.2 ± 0.1 km^3/ka for the eastern part of Tungurahua I not affected by the collapses is obtained, considering the eroded volume of ~16 km^3 during ~80 ka, i.e. since the end of the first edifice construction (Table 3). As Tungurahua II collapsed rapidly after its construction without significant periods of

423 quiescence, and as Tungurahua III is still active, we cannot calculate erosion rates for these
424 edifices.

425 Based on these new results and field observations, we propose in Fig. 3 an update of the
426 Tungurahua geological map (Hall et al., 1999; Bustillos, 2008). Tungurahua II not only
427 consists of the lava flow sequence of the Tiacos unit (Fig. 2), but also crops out in the
428 northern and southwestern flanks. We also propose that the Tungurahua I collapse scar is
429 located to the west of the Tungurahua II scar, as suggested by the location of the upper parts
430 of the Pondoa, Runtún and Ulba plateaux.

431

432 **5. Discussion**

433 *5.1. New groundmass K-Ar ages*

434 *5.1.1 Comparison with previously published ages*

435 The new K-Ar ages of Tungurahua I (Table 1 and Fig. 3b, c and d) are strikingly
436 younger than previously published whole-rock K-Ar ages of 770 ± 5 and 350 ± 4 ka (Barberi
437 et al., 1988), for samples from Tungurahua, but whose location is unknown. Such difference
438 can be explained by the analysis of whole-rock samples that include phenocrysts, which can
439 carry inherited radiogenic argon and/or weathering areas that have experienced loss of
440 potassium. Both phenomena will induce older K-Ar ages. Our results highlight the importance
441 of analysing the groundmass alone, after a thorough mineralogical separation, as previously
442 reported in different contexts, including arc volcanism (e.g., Samper et al., 2007; Germa et al.,
443 2011; Zami et al., 2014). Although unpublished, four $^{40}Ar/^{39}Ar$ ages obtained at the
444 Laboratoire Geoazur (Côte d'Azur University, Nice, France) support our K-Ar ages. Indeed,
445 inverse isochron ages of 27 ± 4 and 104 ± 44 ka (M. Fornari, pers. com.) agree with our ages
446 of 29 ± 2 and 153 ± 14 ka obtained for the same lava flows (PS-117 and PS-110 respectively;
447 Table 1). In addition, two distinct lava flows sampled in the same eruptive phase than PS-99

448 and PS-118 have $^{40}Ar/^{39}Ar$ ages of 99 ± 2 and 252 ± 6 ka (M. Fornari, pers. com.), which are
449 in the range of our K-Ar ages of 79 ± 3 and 293 ± 10 ka, respectively (Table 1). Moreover,
450 most samples from Tungurahua II and III are younger than 15 ka (Table 1), in agreement with
451 their emplacement after the Last Glacial Maximum (Hall et al., 1999; Clapperton, 1990).
452 Although they display a large relative uncertainty, our ages are also consistent with previously
453 published ^{14}C ages of less than ~3 ka for Tungurahua III deposits (Hall et al., 1999; Le Pennec
454 et al., 2008, 2013, 2016).

455 In this southern part of the Ecuadorian arc, within the Inter-andean valley, radiometric
456 ages are available only for Chimborazo and Carihuairazo volcanoes (Fig. 1b). Both were built
457 up since 230 ka, and until Holocene for Chimborazo volcano (Samaniego et al., 2012; Barba
458 et al., 2008). Further south, the construction of the Sangay volcano, the last active edifice of
459 the Eastern Cordillera, started around 500 ka (Monzier et al., 1999; Fig. 1b). Hence, it appears
460 that the construction of Chimborazo, Carihuairazo, Sangay and Tungurahua volcanoes are
461 rather coeval, which suggests a recent development of this part of the arc.

462

463 *5.1.2. Association between ages and volcanic phases*

464 The distribution of our new ages is fairly homogeneous on the scale of the volcano
465 activity, apart from the end of the first edifice construction (Fig. 5). Indeed, the oldest basal
466 lava flows of Tungurahua I have an age of 300 ka, and the edifice remained active until the
467 emplacement of lava flows forming the upper parts of plateaux, at around 80 ka. The edifice
468 collapsed around 33 ka (Le Pennec et al., 2013), but we do not have any sample with an age
469 between 80 ka and the 33 ka destabilization. Tungurahua I activity might have continued
470 between 80 and 33 ka if the lava flows were only emplaced in the summit area or in the
471 western flank that have been destroyed by latter flank collapses, since the plateaus do not
472 seem covered by any younger deposits. Similarly, we did not observe any activity between

246 ± 17 and 188 ± 7 ka (Fig. 5). Although it could be due to a sampling bias, these ~50 ka quiescence periods would be the longest experienced by the volcano. Moreover, owing to the relatively high age-uncertainty of lavas younger than 15 ka (Table 1), and the similar geochemistry observed for the two younger edifices, we cannot determine whether these lavas belong to Tungurahua II or III. Therefore, we rely on stratigraphic relationships observed in the field to associate young samples with a given eruptive phase. Sample PS-109 (7 ± 4 ka) is older than 3 ka and corresponds to Tungurahua II activity (Fig. 3), probably as well as sample PS-107 (5 ± 8 ka), which belongs to a nearby lava flow. Hall et al. (1999) associated the young lava flow at the bottom of the Ulba valley (sampled here as PS-111 and 16EQ19) to Tungurahua III activity based on petrological similarities. However, there are very few mineralogical differences between the two younger edifices (Appendix A). We associate PS-111 and 16EQ19, as well as PS-119 and 16EQ13 (southwestern flank lavas), to Tungurahua II activity (Fig. 3), because Tungurahua III deposits in the sector collapse depression are not thick enough to have overflown into the eastern and southern valleys. Regarding the Baños lava flow (16EQ37; 6 ± 9 ka), there is no place where a clear stratigraphic relationship could be observed between the lava and the ~3 ka collapse deposits (namely the blast deposits associated with the sector collapse). Indeed, these Tungurahua II blast deposits are dated between 2640 ± 45 and 3195 ± 45 BP (^{14}C on charcoal and carbonized twigs), crop out along the Chambo and Puela valleys (Fig. 2) and cover the northern flank of the volcano (Le Pennec et al., 2013), especially Pondoa and Runtún plateaux around Baños city (Fig. 2), but do not crop out above the Baños lava flow. The lava flow originated from a lateral vent (Fig. 3b), and was later covered by an ash deposit dated at 1470 ± 85 BP (^{14}C on charcoal; Hall et al., 1999). Assuming that the Baños lava flow is younger than the blast deposits, we associate the Baños lava flow with the beginning of Tungurahua III activity, in agreement with Hall et al. (1999) and Le Pennec et al. (2016).

The Vizcaya lava flow is coeval with Tungurahua I activity (253 ± 5 ka), but its major and trace contents clearly differ from Tungurahua rocks (Fig. 7; Fig. 9). Hence, this flow cannot be associated with Tungurahua volcano and was rather erupted from an unknown volcanic centre, probably located to the north.

Unfortunately, the southeastern flank could not be sampled and dated in this study. Indeed, access to the Minsas plateau (Fig. 2) was not possible during the erupting period, when our last field trip took place. However, previous major and trace element analyses (Hall et al., 1999; Appendix B) indicate a composition close to those of Ulba upper part (16EQ17; Table 2). Minsas plateau lava geochemistry, morphology and erosion state therefore suggest that the flow is coeval with other Tungurahua I plateau lavas, and was erupted around 80 ka (Fig. 3).

5.2. Location of the ~33 ka sector collapse scar

The succession of construction stages of the volcano and the erosion prevent to accurately determine the location of the Tungurahua I collapse scar. However, morphology analysis of the DEM, and observations made during field campaigns allow us to propose that the northern part of the scar follows the western escarpment of the Pondoa plateau (Fig. 3). Indeed, a "diamond-shaped" plateau, located west of Pondoa, is made of Tungurahua I collapse deposits overlain by Tungurahua II lava flows (Fig. 11). This part of the volcano was therefore destroyed by the first collapse, but was not affected by the second one. Note that such observations are in agreement with the geological map of Hall et al. (1999). The morphology of the southwestern flank, from Patacocha plateau to the second collapse scar, seems to constitute a single unit filling a wide valley (Fig. 3d and Fig. 11d). Indeed, lava flows cover a Tungurahua I breccia deposit, where sample 16EQ12 comes from (Fig. 3a), and no dated lava is there older than 30 ka (Fig. 3d). We therefore propose that the top of the first

(~33 ka) collapse scar is located on the eastern flank at around 3900 m a.s.l., where plateaux slopes change (Fig. 4) forming the lower boundary of the Tiacos unit, and located along the summit part of the Patacocha plateau (Fig. 3).

5.3. Geochemical evolution of the volcanic products

Overall, the lavas of the three successive edifices of Tungurahua volcano show quite similar compositions. Indeed, their silica content varies between 52 and 62 wt.%, and their Mg# between 40 and 60 (Fig. 12a), except for 16EQ17 sample, which is more differentiated than the other lavas, and presents higher content of incompatible elements (Fig. 7; Fig. 9).

The La/Yb ratio varies depending on the depth, composition and nature of the magmas source, fractional crystallization and/or interaction with the mantle (Moyen, 2009). Temporal evolution of the La/Yb ratio for Tungurahua samples (Fig. 12b) shows an overall decrease between 300 and 100 ka, and a significant increase toward the end of Tungurahua I activity, shown by samples younger than 100 ka. During Tungurahua II and III construction, La/Yb contents are relatively scattered, and vary within the range observed for Tungurahua I lavas. Moreover, the La/Sm ratio provides information about the degree of partial melting, and the Sm/Yb ratio is affected by the depth or nature of the magmatic source (e.g., Wilson, 1989; Rollinson, 1993). Fig. 12b shows that these ratios are relatively constant through time for Tungurahua lavas, except a high Sm/Yb content after the ~33 ka collapse (PS-117) and a relatively high La/Sm content towards the end of Tungurahua I construction (16EQ17). Overall, these geochemical evolutions seem to be mainly due to the nature of the magmas. The La/Sm and La/Yb ratios have the same trend than the SiO_2 content as a function of time, except for sample PS-117. The higher ratios correspond to the most differentiated lava flows, such as sample 16EQ17, which is a dacite significantly enriched in the most incompatible elements (LILE, HFSE and LREE; Table 2) compared to other andesite samples. Concerning

548 sample PS-117, the high La/Yb ratio is correlated with its high Sm/Yb ratio, due to its
549 depletion in Dy, Er, Y and Yb (Table 2) that could be related to the heterogeneity of the
550 mantle wedge composition. Large scale sector collapses occurring in volcanic islands may
551 cause an increase of the partial melting rate due to the pressure reduction affecting the magma
552 chamber (e.g., Hildenbrand et al., 2004). On the other hand, the thick crust may prevent sector
553 collapses to affect the deep magmatic source in continental environments. In Ecuador, Robin
554 et al. (2010) observed large geochemical variations just after two major sector collapses in
555 Pichincha volcano lavas (Fig. 1b). The authors infer that new magma batches, associated with
556 new magmatic cycles, may have triggered these sector collapses. We have fewer analyses for
557 Tungurahua volcano, and they are spread over a shorter time scale. However, the
558 geochemistry of Tungurahua lava flows is rather homogeneous for the three edifices and does
559 not seem to be affected by the two observed collapses.

560 Several studies have focused on the evolution through time of Ecuadorian lavas
561 geochemistry, notably for Atacazo (Hidalgo, 2006), Cayambe (Samaniego et al., 2005),
562 Iliniza (Hidalgo et al., 2007), Mojanda-Fuya Fuya (Robin et al., 2009), and Pichincha
563 (Samaniego et al., 2010) volcanoes (Fig. 1b). These edifices are located in the northern part of
564 the Ecuadorian arc, in front of the Carnegie ridge (Fig. 1a). They were constructed since
565 1.3-1.0 Ma until the Holocene, except for Mojanda-Fuya Fuya and Iliniza, which are not
566 precisely dated yet. These edifices present a long-term evolution, between typical
567 calc-alkaline compositions for the oldest lavas, to adakitic compositions for the most recent
568 deposits, which is interpreted as a modification of the sources of the magmas induced by the
569 subduction of the Carnegie ridge, and the subsequent increase of the geothermal gradient. The
570 relatively short duration of Tungurahua activity (about 300 ka), and its location in the
571 southern part of the arc (farther away from the Carnegie ridge than the northern volcanoes),
572 prevent us to identify these long term deep processes, if present. This latter conclusion has

been corroborated by the recent work of Ancellin et al. (2017), who analysed the Sr-Nd-Pb isotopic signature of the Ecuadorian magmas and conclude that magmas from the southern part of the arc (as those of Tungurahua and Sangay volcanoes) do not display a clear subduction slab partial melting component.

5.4. Magmatic productivity and erosion rates

5.4.1. Tungurahua eruptive and erosion rates

The overall volume obtained for the present edifice of Tungurahua (108 ± 30 km3/ka; Table 3 and 4) is similar to the one obtained for Viejo Cayambe (Samaniego et al., 2005), and seems to correspond to a medium size compared to arc volcanoes in general (Table 4; Grosse et al., 2009). However his volume is higher than Ecuadorian Antisana (Hall et al., 2017; Table 4), Imbabura (Le Pennec et al., 2011) and Chimborazo (Samaniego et al., 2012) volcanoes, which are more eroded or younger, and is lower than Rucu Pichincha (Robin et al., 2010) and Mojanda (> 140 km3; Robin et al., 1997) volcanoes, located more to the north (Fig. 1b), and significantly older. Our palaeotopographical reconstructions suggest that Tungurahua I was a volcano with lower sloping upper flanks, while Tungurahua II and III have an exponential shape with a concave profile and steeper slopes (Fig. 4; Fig. 10). The nature of lavas composing these three edifices is very similar and cannot explain this morphological difference. Tungurahua I has been subjected to erosion longer than Tungurahua II and III, and the erosion mainly affected steep slopes of areas near the summit. Less eroded parts, in particularly flanks with low slopes, constitute the present planezes. Our model of Tungurahua I morphology is based on the surface of these planezes, and it does not exclude the possibility that Tungurahua I could have had a similar concave profile as the present edifice at the end of its construction. Assuming that the activity of Tungurahua I ended ~80 ka, we determined the erosion rate by calculating the volume loss between our

598 topographic model at 80 ka and the present-day topography. This was performed only
599 considering the eastern flank, where the remnants of Tungurahua I not affected by sector
600 collapses crop out, and yielded a volume of 16 ± 4 km^3, corresponding to an erosion rate of
601 0.2 ± 0.1 km^3/ka (Table 3). Assuming the long term erosion rate is constant over time, we
602 obtain a total eroded volume of 68 ± 41 km^3 during the construction of Tungurahua I, between
603 293 and 81 ka (PS-118 and PS-116 respectively; Table 1 and 3). Based on our models, the
604 volume of Tungurahua I corresponds to 56 ± 33 km^3 of deposits. In order to take into account
605 the erosion that affected the edifice during its construction phase, we have added the
606 68 ± 41 km^3 eroded volume to calculate the volume of emitted products and the magmatic
607 productivity rate. Our result of 0.6 ± 0.2 km^3/ka (Table 3) thus corresponds to a magmatic
608 production volume of 124 ± 74 km^3 during a period of 212 ka. However, these values should
609 be considered with caution, as the basement elevation under Tungurahua volcano is not well
610 constrained, and the constant erosion rate applied over the whole construction period was
611 most probably variable through time, as a function of the climatic conditions and the nature of
612 outcropping volcanic products. Moreover, we consider that the deep valleys have been dug by
613 erosion, which may have occurred mainly before 30 ka since Tungurahua II lavas outcrop at
614 the bottom of these valleys (Fig. 3). However, these lavas are younger than 15 ka (e.g. sample
615 PS-111), and we cannot quantify the volume of deposits eroded by the Last Glacial
616 Maximum, which occurred between 25 and 15 ka in this region (Clapperton, 1990; Heine,
617 2000). Furthermore, tephra deposits can easily erode when they are not covered with lava
618 flows. It is possible that such deposits existed, but it is difficult to estimate and take into
619 account this volume in our calculations of erosion rates. Similarly, from a calculated volume
620 of 21 ± 4 km^3 obtained for Tungurahua II, added with a volume of 4 ± 2 km^3 for erosion, we
621 obtain a volume of 24 ± 4 km^3 of emitted products, giving an eruptive rate of 0.9 ± 0.2 km^3/ka,
622 similar to Tungurahua I. Finally, the magmatic productivity rate calculated for Tungurahua III

623 (2.5 ± 1.0 km^3/ka; Table 3) is consistent with the eruptive rate of ~1.5 km^3/ka estimated by
624 Hall et al. (1999) over the last 2300 years, for a similar volume to ours. The relatively high
625 production rate calculated for Tungurahua III may be explained by its recent construction and
626 rather continuous activity, compared to the two older edifices, which are averaged over a
627 larger time scale, certainly including periods of quiescence.
628
629 *5.4.2. Comparison between eruptive rates of Tungurahua volcano and other studies*

630 Many phenomena may impact on the magmatic productivity, such as the geodynamic
631 context, the nature and thickness of the crust, or the period of time considered. In a
632 compilation of the magmatic productivity calculated over the world, White et al. (2006)
633 obtained an average rate of 4.4 ± 0.8 km^3/ka for continental crust volcanoes and
634 2.3 ± 0.8 km^3/ka for andesitic edifices. Our eruptive rate of 2.5 km^3/ka, corresponding to
635 Tungurahua III activity (Table 3 and 4), falls within this latter range. Note that the rates of 0.6
636 and 0.9 km^3/ka, obtained here for Tungurahua I and II, respectively (Table 3 and 4), are
637 comparable to the ones obtained on Chimborazo (0.1 to 1 km^3/ka; Samaniego et al., 2012) and
638 Pichincha (~0.6 km^3/ka for both Rucu and Guagua Pichincha; Robin et al., 2010) volcanoes,
639 both also from Ecuador (Fig. 1). Tungurahua eruptive rates are also similar to those from
640 other arc volcanoes, for instance in Chile at Parinacota (~0.3 and 1 km^3/ka for the whole
641 edifice and the young cone, respectively; Hora et al., 2007), Puyehue-Cordón Caulle
642 (0.42 km^3/ka; Singer et al., 2008) and El Misti (0.63 and 2.1 km^3/ka for the whole edifice and
643 peak eruptive rates, respectively; Thouret et al., 2001) volcanoes, which were active since less
644 than 320 ka, or with Ceboruco volcano in Mexico (~0.5 km^3/ka; Frey et al., 2004). However,
645 Tungurahua eruptive rates are significantly higher than at Aucanquilcha volcano in Chile
646 (0.04 and 0.16 km^3/ka for the whole edifice and the highest eruptive rate stage, respectively;
647 Klemetti and Grunder, 2008) and at Tequila volcano in Mexico (0.13 and > 0.24 km^3/ka for

the whole field constructed during the last million years and the youngest cone, respectively; Lewis-Kenedi et al., 2005). These data show that eruptive rates may vary significantly in the same geodynamic context. Moreover, volcanoes which experienced a long period of activity (in the order of one million years) seem to have lower eruptive rates than younger edifices, averaged over shorter times (e.g., Klemetti and Grunder, 2008). The magmatic productivity rates also vary during construction stages of a single edifice, where a few thousand years period of high activity will display a higher eruptive rate than the one averaged on the whole eruptive history of the volcano. Indeed, stratovolcanoes grow in spurts (e.g., Hildreth and Lanphere, 1994; Lewis-Kenedi et al., 2005), with sporadic eruptive pulses, separated by long-time periods of quiescence, producing most of the volcano volume. The magmatic productivity rates averaged over the whole period of construction are therefore systematically lower, such observed for Tungurahua with ~0.4 km^3/ka for the whole volcano (Table 3), while the eruptive rate of the three individual edifices is higher than 0.6 km^3/ka. Magmatic productivity rates of Tungurahua I, II and the whole edifice arelong-term averaged eruptive rates, which include quiescence periods, whereas Tungurahua III, younger than 3 ka, represents a « peak » of activity with a significantly higher eruptive rate (Table 3). A similar picture seems to occur in Peru at Ampato-Sabancaya volcanic complex. Ampato, the older edifice, has an eruptive rate of 0.08-0.09 km^3/ka, whereas it is of 0.6-1.7 km^3/ka for the younger edifice Sabancaya, constructed since 6-10 ka (Samaniego et al., 2016).

As expected, Tungurahua magmatic productivity rates are lower than in a subduction context where the velocity of the plate is faster (5 km^3/ka for Mount Fuji in Japan; Crisp, 1984), and higher than in a subduction context where the convergence rate is slower, as for instance in the Lesser Antilles. Indeed, eruptive rates there vary between 0.13 km^3/ka in Martinique (Mount Pelée; Germa et al., 2015), 0.15 km^3/ka at Montserrat (Harford et al., 2002), and 0.04 to 0.7 km^3/ka in Guadeloupe (Lahitte et al., 2012; Ricci et al., 2015a; 2015b;

673 Table 4). Finally, Tungurahua eruptive rates are lower than those obtained in Argentina for
674 Payún Matrú volcano (4 km^3/ka, averaged over the last 300 ka; Germa et al., 2010), where
675 back-arc extension may have favoured the magma ascent.
676
677 *5.4.3. Comparison between erosion rates of Tungurahua volcano and other studies*
678 Since only a few studies have investigated erosion rates, their relationship with the
679 geodynamic context or the climate variability is still poorly understood. Our erosion rate for
680 Tungurahua I volcano of 0.2 ± 0.1 km^3/ka, equivalent to 6.5 ± 1.7 t/km^2/ka and
681 2.4 ± 0.6 mm/a, calculated for the last 80 ka, is significantly higher than rates obtained in the
682 arid central Andes and in Peru (between 0.01 and 0.11 mm/a; Karátson et al., 2012) or in
683 tropical environments, such as in the Lesser Antilles with0.05 ± 0.02 km^3/ka in Martinique
684 (Germa et al., 2015), and between 0.2 ± 0.2 and 1.4 ± 0.6 t/km^2/ka in Guadeloupe (Ricci et al.,
685 2015a; 2015b) islands. This difference could be explained by the succession of glacial and
686 interglacial periods experienced by Tungurahua volcano, whereas the Antilles islands were
687 only subject to rainfalls. However, morphology and extreme rainfalls experienced by La
688 Réunion island, as well as the faster weathering of basaltic than andesitic lavas (e.g., Gislason
689 et al., 1996; Louvat and Allègre, 1997), may explain its high erosion rate of 1.2 ± 0.4 km^3/ka
690 (Salvany et al., 2012), compared to the one of Tungurahua volcano.
691
692 **6. Conclusions**
693 This study allows us to refine the eruptive history of Tungurahua volcano, which was
694 built in three stages since the last 300 ka. The overall volume calculated for the remaining
695 edifice is ~110 km^3, which corresponds to a mean eruptive rate of ~0.4 km^3/ka. Tungurahua I
696 was a ~125 km^3 andesitic to dacitic stratovolcano, built between 293 ± 10 and 79 ± 3 ka with
697 a magmatic productivity rate of 0.6 ± 0.2 km^3/ka. Pondoa, Runtún, Ulba, Minsas and

698 Patacocha plateaux are present-day remnants of this first edifice. After a ~50 ka long period
699 of quiescence, the first western sector collapse occurred at ~33 ka (Le Pennec et al., 2013).
700 Tungurahua II was built between 29 ± 2 and ~3 ka (Hall et al., 1999; Le Pennec et al., 2013).
701 Around 25 km^3 of volcanic products filled the collapse amphitheatre, with an eruptive rate of
702 0.9 ± 0.2 km^3/ka, similar to those of Tungurahua I. They mainly crop out in the southwestern
703 flank and around Juive Grande area, in the northwestern flank (Fig. 2). Collapse of
704 Tungurahua II western flank was followed by rapid construction of Tungurahua III during the
705 last 3 ka. This third and still active edifice constitutes the western flank of the present-day
706 volcano, and is being built with a relatively high productivity rate of 2.5 ± 1.0 km^3/ka. We
707 also estimated that around 16 km^3 of Tungurahua I volcanic material was eroded since the end
708 of its construction, corresponding to an erosion rate of 0.2 ± 0.1 km^3/ka. The composition of
709 Tungurahua lavas is rather homogeneous, and the magmatic signature of the three edifices do
710 not seem to have been affected by the two sector collapses experienced by the volcano.
711 Moreover, the geochemistry do not show changes in the deep magmatic source as observed
712 for northern Ecuador volcanoes.
713

714 **Acknowledgments**

715 We are particularly grateful to Pablo Grosse for his detailed review and constructive
716 comments, which greatly helped us to improve the clarity of this paper, as well as Joan Marti
717 for his editorial handling. We wish to thank members of Instituto Geofísico, Escuela
718 Politécnica Nacional of Quito for their support, assistance and warm welcome. We also thank
719 J. Bernard and M. Almeida for sampling rocks from upper parts of the volcano, as well as J.
720 Cotten for carrying out the geochemical analyses of the samples presented in Appendix B, and
721 C. Pallares for discussion regarding geochemistry data. This work is part of an Ecuadorian-
722 French cooperation program carried out between the Instituto Geofísico, Escuela Politécnica

Nacional (IGEPN), Quito, Ecuador, and the French Institut de Recherche pour le Développement (IRD), thought its Laboratoire Mixte International "Séismes et Volcans dans les Andes du Nord". Funding was obtained from INSU CNRS TelluS Aleas and LMI IRD programs. This is Laboratoire de Géochronologie Multi-Techniques (LGMT) contribution number XXX and Laboratory of Excellence ClerVolc contribution number XXX.

References

Ancellin, M.-A., Samaniego, P., Vlastélic, I., Nauret, F., Gannoun, A., Hidalgo, S., 2017. Across-arc versus along-arc Sr-Nd-Pb isotope variations in the Ecuadorian volcanic arc. Geochem. Geophys. Geosystems 18. doi:10.1002/2016GC006679

Arellano, S.R., Hall, M., Samaniego, P., Le Pennec, J.-L., Ruiz, A., Molina, I., Yepes, H., 2008. Degassing patterns of Tungurahua volcano (Ecuador) during the 1999–2006 eruptive period, inferred from remote spectroscopic measurements of SO2 emissions. J. Volcanol. Geotherm. Res. 176, 151–162. doi:10.1016/j.jvolgeores.2008.07.007

Aspden, J.A., Litherland, M., 1992. The geology and Mesozoic collisional history of the Cordillera Real, Ecuador. Tectonophysics 205, 187–204.

Barba, D., Robin, C., Samaniego, P., Eissen, J.-P., 2008. Holocene recurrent explosive activity at Chimborazo volcano (Ecuador). J. Volcanol. Geotherm. Res. 176, 27–35. doi:10.1016/j.jvolgeores.2008.05.004

Barberi, F., Coltelli, M., Ferrara, G., Innocenti, F., Navarro, J.M., Santacroce, R., 1988. Plio-Quaternary Volcanism in Ecuador. Geochem. Mag. 125, 1–14.

Bernard, B., Andrade, D., 2011. Volcanes Cuaternarios del Ecuador Continental, Instituto Geofísico - Escuela Politécnica Nacional and Institut de Recherche pour le Développement, Poster Informativo.

Bernard, J., Kelfoun, K., Le Pennec, J.-L., Vallejo Vargas, S., 2014. Pyroclastic flow erosion and bulking processes: comparing field-based vs. modeling results at Tungurahua volcano, Ecuador. Bull. Volcanol. 76. doi:10.1007/s00445-014-0858-y

Bourdon, E., Eissen, J.P., Gutscher, M.A., Monzier, M., Hall, M.L., Cotten, J., 2003. Magmatic response to early aseismic ridge subduction: the Ecuadorian margin case (South America). Earth Planet. Sci. Lett. 205, 123–128.

Bryant, J.A., 2006. Geochemical Constraints on the Origin of Volcanic Rocks from the Andean Northern Volcanic Zone, Ecuador. J. Petrol. 47, 1147–1175. doi:10.1093/petrology/egl006

Bustillos, J.E., 2008. Las avalanchas de escombros en el sector del volcán Tungurahua (MSC). Facultad de ingeniería en geología y petróleos - Escuela Politécnica Nacional, Quito.

Bustillos, J., Samaniego, P., Robin, C., Barba, D., Ramón, P., Le Pennec, J.-L., 2011. Las avalanchas de escombros del volcán Tungurahua, in: 7mas Jornadas en Ciencias de la Tierra y Primer encuentro sobre Riesgos y Desastres, Quito 2011.

Cassignol, C., Gillot, P.-Y., 1982. Range and effectiveness of unspiked potassium-argon dating: experimental groundwork and application. Odin GS Ed Numer. Dating Stratigr. John Wiley & Sons, New York, 159–179.

765 Castillo, P.R., Janney, P.E., Solidum, R.U., 1999. Petrology and geochemistry of Camiguin
766 Island, southern Philippines: insights to the source of adakites and other lavas in a
767 complex arc setting. Contrib. Mineral. Petrol. 134, 33–51.
768 Champenois, J., Pinel, V., Baize, S., Audin, L., Jomard, H., Hooper, A., Alvarado, A., Yepes,
769 H., 2014. Large-scale inflation of Tungurahua volcano (Ecuador) revealed by
770 Persistent Scatterers SAR interferometry. Geophys. Res. Lett. 41, 5821–5828.
771 doi:10.1002/2014GL060956
772 Chiaradia, M., Barnes, J.D., Cadet-Voisin, S., 2014. Chlorine stable isotope variations across
773 the Quaternary volcanic arc of Ecuador. Earth Planet. Sci. Lett. 396, 22–33.
774 doi:10.1016/j.epsl.2014.03.062
775 Clapperton, C.M., 1990. Glacial and volcanic geomorphology of the Chimborazo-
776 Carihuairazo Massif, Ecuadorian Andes. Trans. R. Soc. Edinburg Earth Sci. 81, 91–
777 116.
778 Cotten, J., Le Dez, A., Bau, M., Caroff, M., Maury, R.C., Dulski, P., Fourcade, S., Bohn, M.,
779 Brousse, R., 1995. Origin of anomalous rare-earth element and yttrium enrichments in
780 subaerially exposed basalts: Evidence from French Polynesia. Chem. Geol. 119, 115–
781 138.
782 Crisp, J.A., 1984. Rates of magma emplacement and volcanic output. J. Volcanol. Geotherm.
783 Res. 20, 177–211.
784 Deino, A., Potts, R., 1992. Age-probability spectra for examination of single-crystal
785 40Ar39Ar dating results: Examples from Olorgesailie, southern Kenya Rift. Quat. Int.
786 13, 47–53.
787 DeMets, C., Gordon, R.G., Argus, D.F., Stein, S., 1990. Current plate motions. Geophys. J.
788 Int. 101, 425–478.
789 Frey, H.M., Lange, R.A., Hall, C.M., Delgado-Granados, H., 2004. Magma eruption rates
790 constrained by 40Ar/39Ar chronology and GIS for the Ceboruco-San Pedro volcanic
791 field, western Mexico. Geol. Soc. Am. Bull. 116, 259–276. doi: 10.1130/B25321.1
792 Germa, A., Quidelleur, X., Gillot, P.Y., Tchilinguirian, P., 2010. Volcanic evolution of the
793 back-arc Pleistocene Payun Matru volcanic field (Argentina). J. South Am. Earth Sci.
794 29, 717–730. doi:10.1016/j.jsames.2010.01.002
795 Germa, A., Quidelleur, X., Lahitte, P., Labanieh, S., Chauvel, C., 2011. The K–Ar Cassignol–
796 Gillot technique applied to western Martinique lavas: A record of Lesser Antilles arc
797 activity from 2 Ma to Mount Pelée volcanism. Quat. Geochronol. 6, 341–355.
798 doi:10.1016/j.quageo.2011.02.001
799 Germa, A., Lahitte, P., Quidelleur, X., 2015. Construction and destruction of Mont Pelée
800 volcano: Volumes and rates constrained from a geomorphological model of evolution:
801 Construction and Destruction of Mont Pelée. J. Geophys. Res. Earth Surf. 120, 1206–
802 1226. doi:10.1002/2014JF003355
803 Gillot, P.-Y., Cornette, Y., 1986. The Cassignol technique for Potassium-Argon dating,
804 precision and accuracy: exemples from the late Pleistocene to recent volcanics from
805 southern Italy. Chem. Geol. Isot. Geosci. Sect. 59, 205–222.
806 Gillot, P.-Y., Cornette, Y., Max, N., Floris, B., 1992. Two reference materials, trachytes
807 MDO-G and ISH-G, for argon dating (K-Ar and 40Ar/39Ar) of Pleistocene and
808 Holocene rocks. Geostand. Newsl. 16, 55–60.
809 Gillot, P.-Y., Hildenbrand, A., Lefèvre, J.-C., Albore-Livadie, C., 2006. The K/Ar dating
810 method : principle, analytical techniques, and application to Holocene volcanic
811 eruptions in Southern Italy. Acta Vulcanol. 18, 55–66.
812 Gislason, S.R., Arnorsson, S., Armannsson, H., 1996. Chemical weathering of basalt in
813 Southwest Iceland; effects of runoff, age of rocks and vegetative/glacial cover. Am. J.
814 Sci. 296, 837–907.

Grosse, P., van Wyk de Vries, B., Petrivonic, I.A., Euillades, P.A., Alvarado, G.E., 2009. Morphometry and evolution of arc volcanoes. Geology 37, 651–654. doi:10.1130/G25734A.1

Hall, M.L., Robin, C., Beate, B., Mothes, P., Monzier, M., 1999. Tungurahua Volcano, Ecuador: structure, eruptive history and hazards. J. Volcanol. Geotherm. Res. 91, 1–21.

Hall, M.L., Samaniego, P., Le Pennec, J.L., Johnson, J.B., 2008. Ecuadorian Andes volcanism: A review of Late Pliocene to present activity. J. Volcanol. Geotherm. Res. 176, 1–6. doi:10.1016/j.jvolgeores.2008.06.012

Hall, M.L., Steele, A.L., Mothes, P.A., Ruiz, M.C., 2013. Pyroclastic density currents (PDC) of the 16–17 August 2006 eruptions of Tungurahua volcano, Ecuador: Geophysical registry and characteristics. J. Volcanol. Geotherm. Res. 265, 78–93. doi:10.1016/j.jvolgeores.2013.08.011

Hall, M.L., Mothes, P.A., Samaniego, P., Militzer, A., Beate, B., Ramón, P., Robin, C., 2017. Antisana volcano: A representative andesitic volcano of the eastern cordillera of Ecuador: Petrography, chemistry, tephra and glacial stratigraphy. J. South Am. Earth Sci. 73, 50–64. doi:10.1016/j.jsames.2016.11.005

Harford, C.L., Pringle, M.S., Sparks, R.S.J., Young, S.R., 2002. The volcanic evolution of Montserrat using 40Ar/39Ar geochronology. Geol. Soc. Lond. Mem. 21, 93–113. doi:10.1144/GSL.MEM.2002.021.01.05

Heine, K., 2000. Tropical South America during the last glacial maximum: evidence from glacial, periglacial and fluvial records. Quat. Int. 72, 7–21.

Hess, J.C., Lippolt, H.J., 1994. Compilation of K-Ar measurements on HD-B1 standard biotite, 1994 status report. Phaneroz. Time Scale, Bull. Liais. Inform. IUGS Subcomm. Geochronol. 122.

Hidalgo, S., 2006. Les interactions entre magmas calco-alcalins “classiques” et adakitiques : exemple du complexe volcanique Atacazo-Ninahuilca (Equateur). Université Blaise Pascal-Clermont-Ferrand II.

Hidalgo, S., Monzier, M., Martin, H., Chazot, G., Eissen, J.-P., Cotten, J., 2007. Adakitic magmas in the Ecuadorian Volcanic Front: Petrogenesis of the Iliniza Volcanic Complex (Ecuador). J. Volcanol. Geotherm. Res. 159, 366–392. doi:10.1016/j.jvolgeores.2006.07.007

Hidalgo, S., Gerbe, M.C., Martin, H., Samaniego, P., Bourdon, E., 2012. Role of crustal and slab components in the Northern Volcanic Zone of the Andes (Ecuador) constrained by Sr–Nd–O isotopes. Lithos 132–133, 180–192. doi:10.1016/j.lithos.2011.11.019

Hidalgo, S., Battaglia, J., Arellano, S., Steele, A., Bernard, B., Bourquin, J., Galle, B., Arrais, S., Vásconez, F., 2015. SO2 degassing at Tungurahua volcano (Ecuador) between 2007 and 2013: Transition from continuous to episodic activity. J. Volcanol. Geotherm. Res. 298, 1–14. doi:10.1016/j.jvolgeores.2015.03.022

Hildenbrand, A., Gillot, P.-Y., Le Roy, I., 2004. Volcano-tectonic and geochemical evolution of an oceanic intra-plate volcano: Tahiti-Nui (French Polynesia). Earth Planet. Sci. Lett. 217, 349–365. doi:10.1016/S0012-821X(03)00599-5

Hildreth, W., Lanphere, M.A., 1994. Potassium-argon geochronology of a basalt-andesite-dacite arc system: The Mount Adams volcanic field, Cascade Range of southern Washington. Geol. Soc. Am. Bull. 106, 1413–1429.

Hora, J.M., Singer, B.S., Wörner, G., 2007. Volcano evolution and eruptive flux on the thick crust of the Andean Central Volcanic Zone: 40Ar/39Ar constraints from Volcan Parinacota, Chile. Geol. Soc. Am. Bull. 119, 343–362. doi:10.1130/B25954.1

Karátson, D., Telbisz, T., Wörner, G., 2012. Erosion rates and erosion patterns of Neogene to Quaternary stratovolcanoes in the Western Cordillera of the Central Andes: An SRTM DEM based analysis. Geomorphology 139–140, 122–135. doi:10.1016/j.geomorph.2011.10.010

Klemetti, E.W., Grunder, A.L., 2008. Volcanic evolution of Volcán Aucanquilcha: a long-lived dacite volcano in the Central Andes of northern Chile. Bull. Volcanol. 70, 633–650. doi:10.1007/s00445-007-0158-x

Kumagai, H., Placios, P., Ruiz, M., Yepes, H., Kozono, T., 2011. Ascending seismic source during an explosive eruption at Tungurahua volcano, Ecuador. Geophys. Res. Lett. 38, 5. doi:10.1029/2010GL045944

Lahitte, P., Samper, A., Quidelleur, X., 2012. DEM-based reconstruction of southern Basse-Terre volcanoes (Guadeloupe archipelago, FWI): Contribution to the Lesser Antilles Arc construction rates and magma production. Geomorphology 136, 148–164. doi:10.1016/j.geomorph.2011.04.008

Lavigne, F., Degeai, J.-P., Komorowski, J.-C., Guillet, S., Robert, V., Lahitte, P., Oppenheimer, C., Stoffel, M., Vidal, C.M., Surono, Pratomo, I., Wassmer, P., Hajdas, I., Hadmoko, D.S., de Belizal, E., 2013. Source of the great A.D. 1257 mystery eruption unveiled, Samalas volcano, Rinjani Volcanic Complex, Indonesia. Proc. Natl. Acad. Sci. 110, 16742–16747. doi:10.1073/pnas.1307520110

Le Pennec, J.-L., Hall, M.L., Robin, C., Bartomioli, E., 2006. Tungurahua volcano, Late Holocene Activity.

Le Pennec, J.-L., Jaya, D., Samaniego, P., Ramón, P., Moreno Yánez, S., Egred, J., van der Plicht, J., 2008. The AD 1300–1700 eruptive periods at Tungurahua volcano, Ecuador, revealed by historical narratives, stratigraphy and radiocarbon dating. J. Volcanol. Geotherm. Res. 176, 70–81. doi:10.1016/j.jvolgeores.2008.05.019

Le Pennec, J.L., Ruiz, A.G., Eissen, J.P., Hall, M.L., Fornari, M., 2011. Identifying potentially active volcanoes in the Andes: Radiometric evidence for late Pleistocene-early Holocene eruptions at Volcán Imbabura, Ecuador. J. Volcanol. Geotherm. Res. 206, 121–135. doi:10.1016/j.jvolgeores.2011.06.002

Le Pennec, J.-L., Ruiz, G.A., Ramón, P., Palacios, E., Mothes, P., Yepes, H., 2012. Impact of tephra falls on Andean communities: The influences of eruption size and weather conditions during the 1999–2001 activity of Tungurahua volcano, Ecuador. J. Volcanol. Geotherm. Res. 217–218, 91–103. doi:10.1016/j.jvolgeores.2011.06.011

Le Pennec, J.-L., De Saulieu, G., Samaniego, P., Jaya, D., Gailler, L., 2013. A Devastating Plinian Eruption at Tungurahua Volcano Reveals Formative Occupation at ~1100 cal BC in Central Ecuador. Radiocarbon 55, 1199–1214.

Le Pennec, J.-L., Ramón, P., Robin, C., Almeida, E., 2016. Combining historical and 14C data to assess pyroclastic density current hazards in Baños city near Tungurahua volcano (Ecuador). Quat. Int. 394, 98–114. doi:10.1016/j.quaint.2015.06.052

Lewis-Kenedi, C.B., Lange, R.A., Hall, C.M., Delgado-Granados, H., 2005. The eruptive history of the Tequila volcanic field, western Mexico: ages, volumes, and relative proportions of lava types. Bull. Volcanol. 67, 391–414. doi:10.1007/s00445-004-0377-3

Louvat, P., Allègre, C.J., 1997. Present denudation rates on the island of Reunion determined by river geochemistry: basalt weathering and mass budget between chemical and mechanical erosions. Geochim. Cosmochim. Acta 61, 3645–3669.

Martin, H., Moyen, J.-F., Guitreau, M., Blichert-Toft, J., Le Pennec, J.-L., 2014. Why Archaean TTG cannot be generated by MORB melting in subduction zones. Lithos 198–199, 1–13. doi:10.1016/j.lithos.2014.02.017

912 Molina, I., Kumagai, H., Le Pennec, J.-L., Hall, M., 2005. Three-dimensional P-wave velocity
913 structure of Tungurahua Volcano, Ecuador. J. Volcanol. Geotherm. Res. 147, 144–
914 156. doi:10.1016/j.jvolgeores.2005.03.011
915 Monzier, M., Robin, C., Samaniego, P., Hall, M.L., Cotten, J., Mothes, P., Arnaud, N., 1999.
916 Sanguay volcano, Ecuador: structural development, present activity and petrology. J.
917 Volcanol. Geotherm. Res. 90, 49–79.
918 Moyen, J.-F., 2009. High Sr/Y and La/Yb ratios: The meaning of the "adakitic signature."
919 Lithos 112, 556–574. doi:10.1016/j.lithos.2009.04.001
920 Myers, M.L., Geist, D.J., Rowe, M.C., Harpp, K.S., Wallace, P.J., Dufek, J., 2014.
921 Replenishment of volatile-rich mafic magma into a degassed chamber drives mixing
922 and eruption of Tungurahua volcano. Bull. Volcanol. 76. doi:10.1007/s00445-014-
923 0872-0
924 Peccerillo, A., Taylor, S.R., 1976. Geochemistry of Eocene calc-alkaline volcanic rocks from
925 the Kastamonu area, northern Turkey. Contrib. Mineral. Petrol. 58, 63–81.
926 Quidelleur, X., Gillot, P.-Y., Soler, V., Lefèvre, J.-C., 2001. K/Ar dating extended into the
927 last millennium: application to the youngest effusive episode of the Teide volcano
928 (Spain). Geophys. Res. Lett. 28, 3067–3070.
929 Raczek, I., Stoll, B., Hofmann, A.W., Peter Jochum, K., 2001. High-Precision Trace Element
930 Data for the USGS Reference Materials BCR-1, BCR-2, BHVO-1, BHVO-2, AGV-1,
931 AGV-2, DTS-1, DTS-2, GSP-1 and GSP-2 by ID-TIMS and MIC-SSMS. Geostand.
932 Newsl. 25, 77–86.
933 Ricci, J., Lahitte, P., Quidelleur, X., 2015a. Construction and destruction rates of volcanoes
934 within tropical environment: Examples from the Basse-Terre Island (Guadeloupe,
935 Lesser Antilles). Geomorphology 228, 597–607. doi:10.1016/j.geomorph.2014.10.002
936 Ricci, J., Quidelleur, X., Lahitte, P., 2015b. Volcanic evolution of central Basse-Terre Island
937 revisited on the basis of new geochronology and geomorphology data. Bull. Volcanol.
938 77. doi:10.1007/s00445-015-0970-7
939 Robin, C., Hall, M.L., Jimenez, M., Monzier, M., Escobar, P., 1997. Mojanda volcanic
940 complex (Ecuador): Development of two adjacent contemporaneous volcanoes with
941 contrasting eruptive styles and magmatic suites. J. South Am. Earth Sci. 10, 345–359.
942 Robin, C., Eissen, J.-P., Samaniego, P., Martin, H., Hall, M., Cotten, J., 2009. Evolution of
943 the late Pleistocene Mojanda–Fuya Fuya volcanic complex (Ecuador), by progressive
944 adakitic involvement in mantle magma sources. Bull. Volcanol. 71, 233–258.
945 doi:10.1007/s00445-008-0219-9
946 Robin, C., Samaniego, P., Le Pennec, J.-L., Fornari, M., Mothes, P., van der Plicht, J., 2010.
947 New radiometric and petrological constraints on the evolution of the Pichincha
948 volcanic complex (Ecuador). Bull. Volcanol. 72, 1109–1129. doi:10.1007/s00445-
949 010-0389-0
950 Rollinson, H., 1993. Using geochemical data: evaluation, presentation, interpretation.
951 Longman Scientific and Technical, London, ISBN: 0-582-06701-4, pp. 166-168.
952 Salvany, T., Lahitte, P., Nativel, P., Gillot, P.-Y., 2012. Geomorphic evolution of the Piton
953 des Neiges volcano (Réunion Island, Indian Ocean): Competition between volcanic
954 construction and erosion since 1.4 Ma. Geomorphology 136, 132–147.
955 doi:10.1016/j.geomorph.2011.06.009
956 Samaniego, P., Martin, H., Robin, C., Monzier, M., 2002. Transition from calc-alkalic to
957 adakitic magmatism at Cayambe volcano, Ecuador: insights into slab melts and mantle
958 wedge interactions. Geology 30, 967–970.
959 Samaniego, P., Martin, H., Monzier, M., Robin, C., Fornari, M., Eissen, J.-P., Cotten, J.,
960 2005. Temporal Evolution of Magmatism in the Northern Volcanic Zone of the

961 Andes: The Geology and Petrology of Cayambe Volcanic Complex (Ecuador). J.
962 Petrol. 46, 2225–2252. doi:10.1093/petrology/egi053
963 Samaniego, P., Le Pennec, J.L., Barba, D., Hall, M.L., Robin, C., Mothes, P., Yepes, H.,
964 Troncoso, L., Jaya, D., 2008. Mapa de los peligros potenciales del volcán Tungurahua,
965 1:50000, 3rd edition (in spanish).
966 Samaniego, P., Robin, C., Chazot, G., Bourdon, E., Cotten, J., 2010. Evolving metasomatic
967 agent in the Northern Andean subduction zone, deduced from magma composition of
968 the long-lived Pichincha volcanic complex (Ecuador). Contrib. Mineral. Petrol. 160,
969 239–260. doi:10.1007/s00410-009-0475-5
970 Samaniego, P., Le Pennec, J.-L., Robin, C., Hidalgo, S., 2011. Petrological analysis of the
971 pre-eruptive magmatic process prior to the 2006 explosive eruptions at Tungurahua
972 volcano (Ecuador). J. Volcanol. Geotherm. Res. 199, 69–84.
973 doi:10.1016/j.jvolgeores.2010.10.010
974 Samaniego, P., Barba, D., Robin, C., Fornari, M., Bernard, B., 2012. Eruptive history of
975 Chimborazo volcano (Ecuador): A large, ice-capped and hazardous compound
976 volcano in the Northern Andes. J. Volcanol. Geotherm. Res. 221–222, 33–51.
977 doi:10.1016/j.jvolgeores.2012.01.014
978 Samper, A., Quidelleur, X., Lahitte, P., Mollex, D., 2007. Timing of effusive volcanism and
979 collapse events within an oceanic arc island: Basse-Terre, Guadeloupe archipelago
980 (Lesser Antilles Arc). Earth Planet. Sci. Lett. 258, 175–191.
981 doi:10.1016/j.epsl.2007.03.030
982 Samper, A., Quidelleur, X., Boudon, G., Le Friant, A., Komorowski, J.C., 2008. Radiometric
983 dating of three large volume flank collapses in the Lesser Antilles Arc. J. Volcanol.
984 Geotherm. Res. 176, 485–492. doi: 10.1016/j.jvolgeores.2008.04.018
985 Samper, A., Quidelleur, X., Komorowski, J.-C., Lahitte, P., Boudon, G., 2009. Effusive
986 history of the Grande Découverte Volcanic Complex, southern Basse-Terre
987 (Guadeloupe, French West Indies) from new K–Ar Cassignol–Gillot ages. J. Volcanol.
988 Geotherm. Res. 187, 117–130. doi:10.1016/j.jvolgeores.2009.08.016
989 Schiano, P., Monzier, M., Eissen, J.-P., Martin, H., Koga, K.T., 2010. Simple mixing as the
990 major control of the evolution of volcanic suites in the Ecuadorian Andes. Contrib.
991 Mineral. Petrol. 160, 297–312. doi:10.1007/s00410-009-0478-2
992 Singer, B.S., Jicha, B.R., Harper, M.A., Naranjo, J.A., Lara, L.E., Moreno-Roa, H., 2008.
993 Eruptive history, geochronology, and magmatic evolution of the Puyehue-Cordon
994 Caulle volcanic complex, Chile. Geol. Soc. Am. Bull. 120, 599–618.
995 doi:10.1130/B26276.1
996 Smith, W.H.F., Sandwell, D.T., 1997. Global Sea Floor Topography from Satellite Altimetry
997 and Ship Depth Soundings. Science 277, 1956–1962.
998 Steiger, R.H., Jäger, E., 1977. Subcommission on geochronology: convention on the use of
999 decay constants in geo- and cosmochronology. Earth Planet. Sci. Lett. 36, 359–362.
1000 Sun, S.-s., McDonough, W.F., 1989. Chemical and isotopic systematics of oceanic basalts:
1001 implications for mantle composition and processes. Geol. Soc. Lond. Spec. Publ. 42,
1002 313–345. doi:10.1144/GSL.SP.1989.042.01.19
1003 Thouret, J.-C., Finizola, A., Fornari, M., Legeley-Padovani, A., Suni, J., Frechen, M., 2001.
1004 Geology of El Misti volcano near the city of Arequipa, Peru. Geol. Soc. Am. Bull.
1005 113, 1593–1610.
1006 White, S.M., Crisp, J.A., Spera, F.J., 2006. Long-term volumetric eruption rates and magma
1007 budgets. Geochem. Geophys. Geosystems 7. doi:10.1029/2005GC001002
1008 Wilson, M., 1989. Igneous petrogenesis. A global tectonic approach. Chapman and Hall,
1009 London, Glasgow, New York, Tokyo, Melbourne, Madras. ISBN: 0-412-53310-3, pp.
1010 51-97.

1011 Zami, F., Quidelleur, X., Ricci, J., Lebrun, J.-F., Samper, A., 2014. Initial sub-aerial volcanic
1012 activity along the central Lesser Antilles inner arc: New K–Ar ages from Les Saintes
1013 volcanoes. J. Volcanol. Geotherm. Res. 287, 12–21.
1014 doi:10.1016/j.jvolgeores.2014.09.011
1015

Figure captions

Fig. 1:

a) Regional setting of Ecuador, showing main tectonic structures and geodynamic context of the Northern Volcanic Zone of the Andes. Arrows indicate the direction of plate motion (DeMets et al., 1990). Bathymetry image is from GeoMapApp, using data of Smith and Sandwell (1997). Red triangle represents location of Tungurahua volcano. b) Map of Ecuadorian volcanic arc, modified from Hall et al. (2008). Volcanoes are distributed along the Western Cordillera (volcanic front, represented in blue), the Inter-andean valley (green), the Eastern Cordillera (orange) and the back arc (red). Quito, the capital city, is represented in grey. Tungurahua volcano is surrounded by heavy black borders. At: Atacazo; Ca: Carihuairazo; Cay: Cayambe; Ch: Chimborazo; Co: Cotopaxi; Il:Iliniza; Mo: Mojanda; Pi: Pichincha; Re: Reventador; Sa: Sangay.

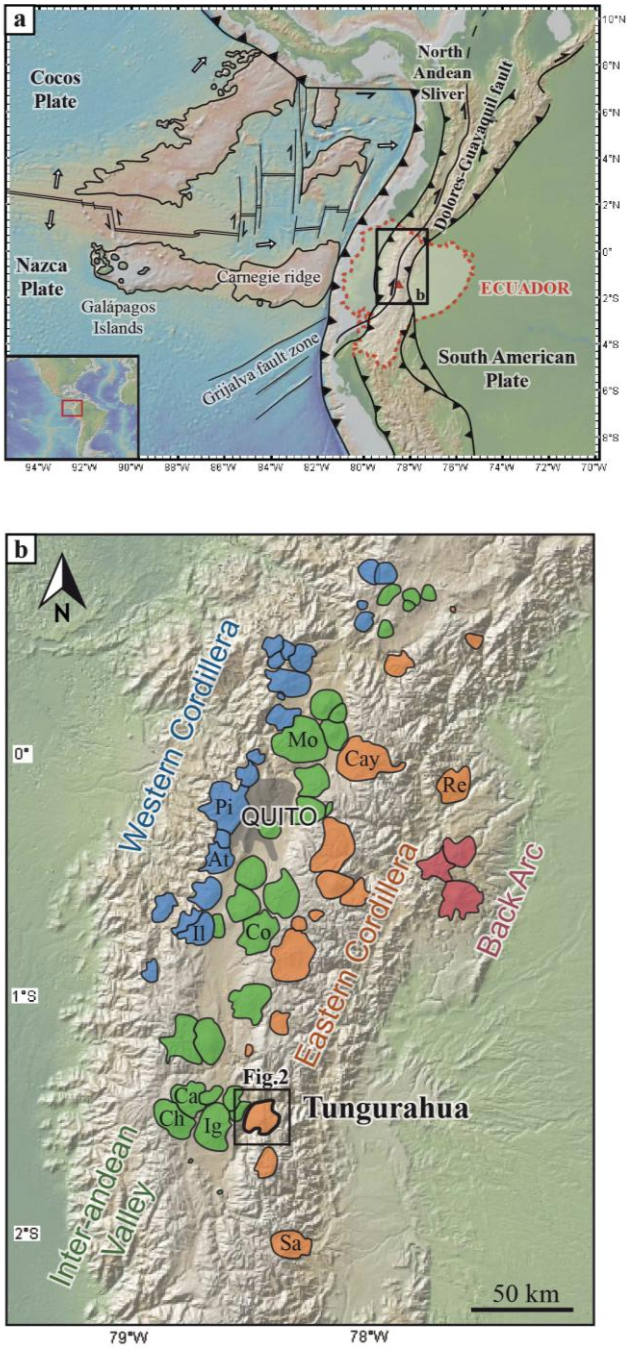

Fig. 2:

Shaded view of the Shuttle Radar Topography Mission (SRTM) Digital Elevation Model (DEM; 30-m resolution) of Tungurahua volcano and places mentioned in the text (location is indicated on Fig.1b). Coordinates are in Universal Transverse Mercator (UTM; zone 17). Mulmul and Huisla are neighbour volcanoes located in the Inter-andean valley. Blue lines represent main rivers and thin black lines the boundary of plateaux upper surfaces. Tiacos unit corresponds to a 80-100 m-thick sequence of Tungurahua II lava flows that cover older lavas of Tungurahua I (Hall et al., 1999). Vizcaya lava flow extends over at least 5 km along the valley north of Tungurahua, from an unknown source.

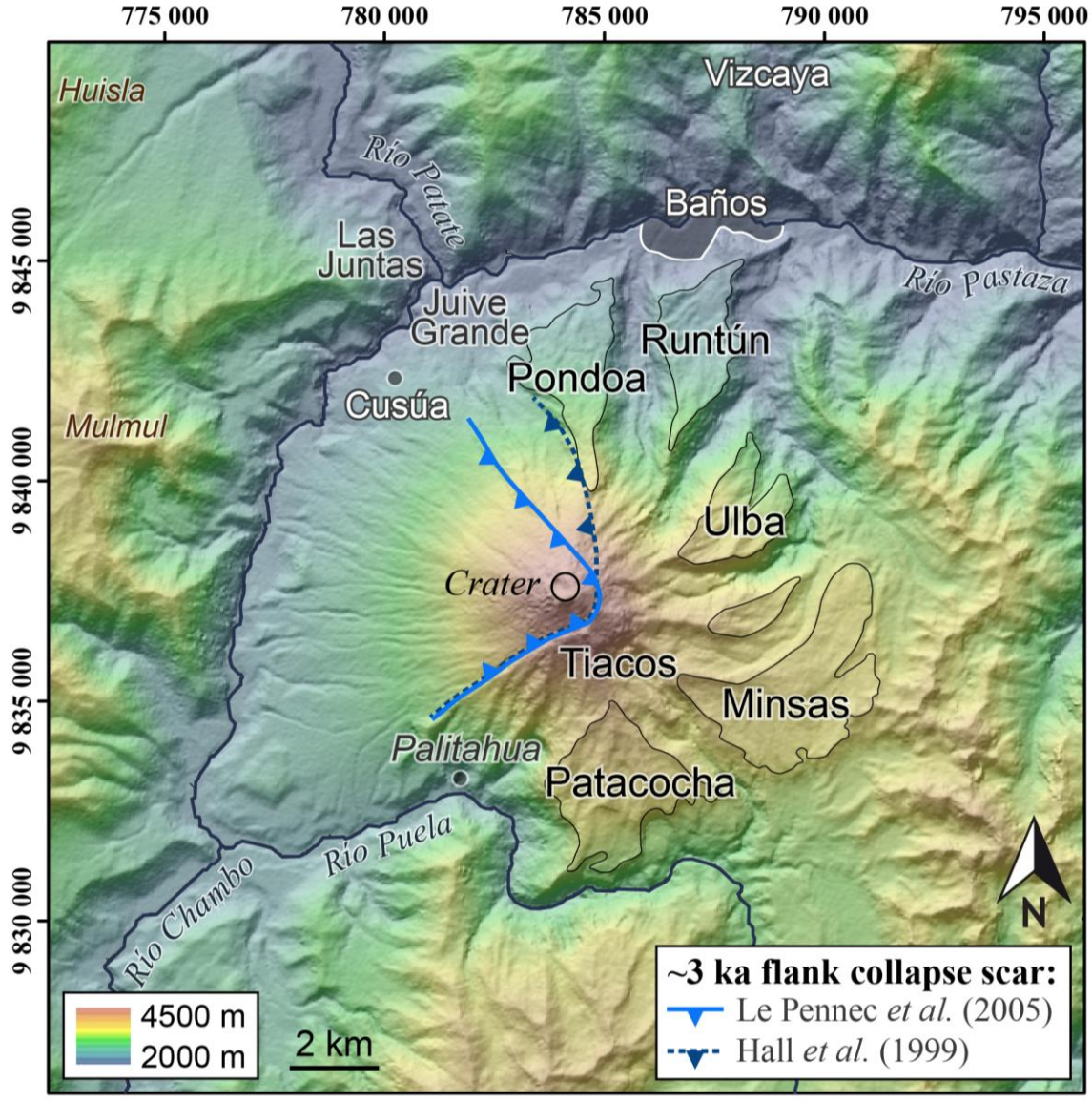

Fig. 3:

a) Revised geological map of Tungurahua volcano reported on shaded SRTM DEM after considering our new ages and field observations. Sample locations presented in this study are indicated by a black (K-Ar dated samples) or a white (non-dated samples) symbol. All samples have been analysed for major and trace elements. Geological units are updated from Hall et al. (1999), and the collapse deposits cartography is presented in Bustillos et al. (2011). b), c), and d) are detailed views of the northern, southern, and eastern flanks respectively, showing location of the new K-Ar ages.

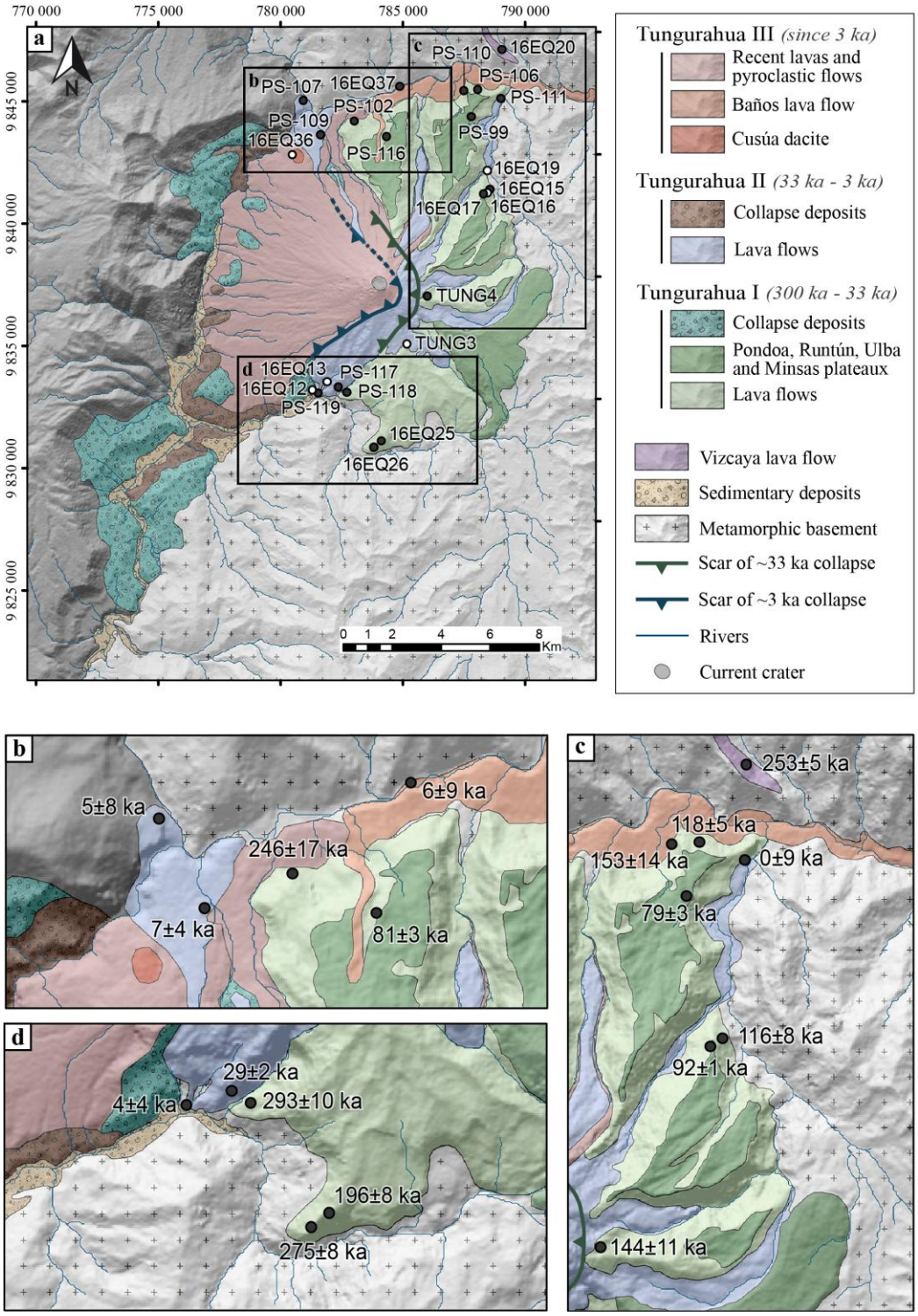

Fig. 4:

a) Current elevation profiles of the three edifices, with their respective topographic models before erosion. The location of the profiles is indicated in Fig. 4b. Asymmetrical altitude is due to the basement located higher to the west. b) Selected points used for reconstructions reported on shaded DEM of Tungurahua volcano. c) 3D view with the same selected point.

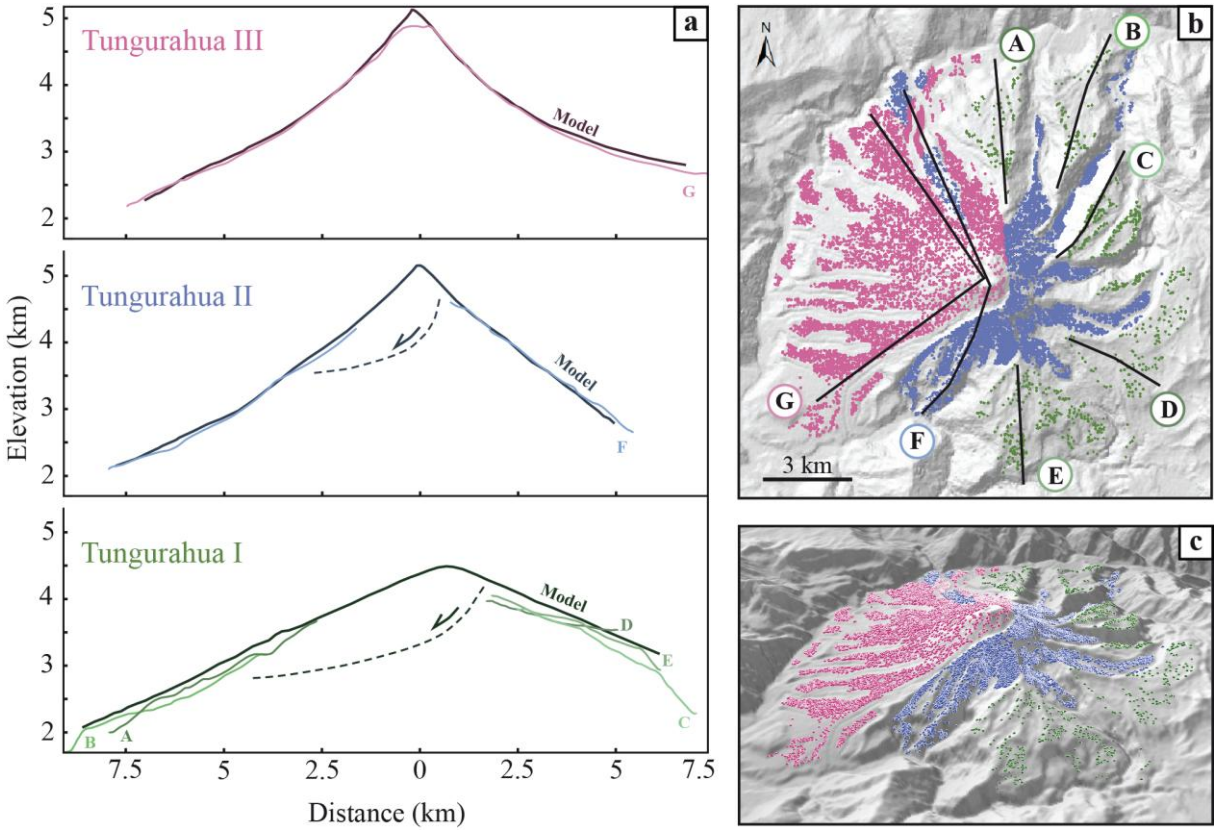

Fig. 5:

Age-probability spectrum, outlining potential gaps of activity between 78 and 33 ka for Tungurahua I, and between 27 and 15 ka for Tungurahua II. The method used to calculate the relative probability is detailed in Deino and Potts (1992).The ages are plotted above with their 1σ uncertainty error bars. Green dotted line: ~33 ka collapse; blue dotted line: ~3 ka collapse.

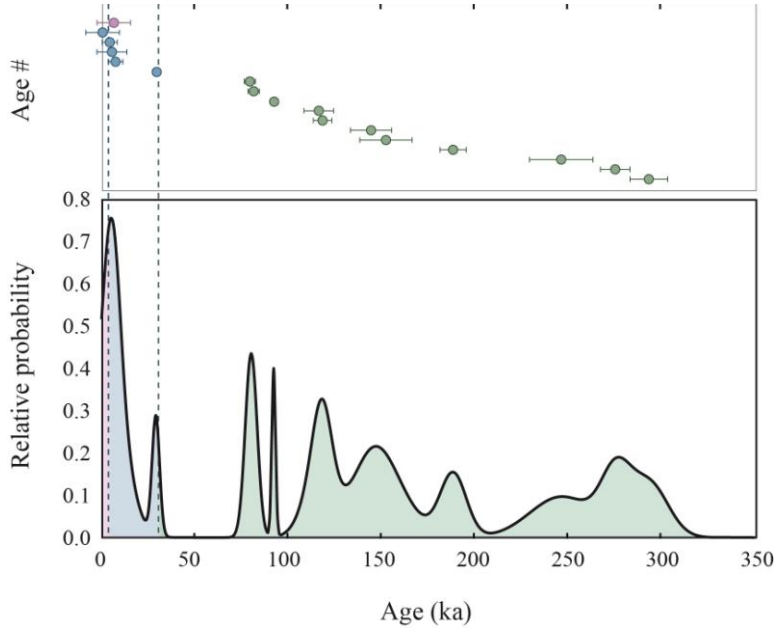

Fig. 6:

K_2O vs. SiO_2 diagram (Peccerillo and Taylor, 1976). Hatched gray domain represent whole rock data of Eastern Cordillera volcanoes, from the GEOROC database (http://georoc.mpch-mainz.gwdg.de/ ; using Samaniego et al. (2005), Bryant (2006), Hidalgo et al. (2012) and Chiaradia et al. (2014) studies). Data for Tungurahua I (green field), Tungurahua II (blue) and Tungurahua III (pink) originate from Schiano et al. (2010); Samaniego et al. (2011) and Le Pennec et al. (2013), and new data presented in Appendix B. Due to small amount of Tungurahua II outcrops, the blue domain was drawn from a smaller number of measurements. The inset represents the compositional fields of blocks belonging to Tungurahua I (turquoise) and II (brown) sector collapse deposits. HK: high-K calc-alkaline serie, MK: medium-K calc-alkaline serie, LK: low-K calc-alkaline serie. .

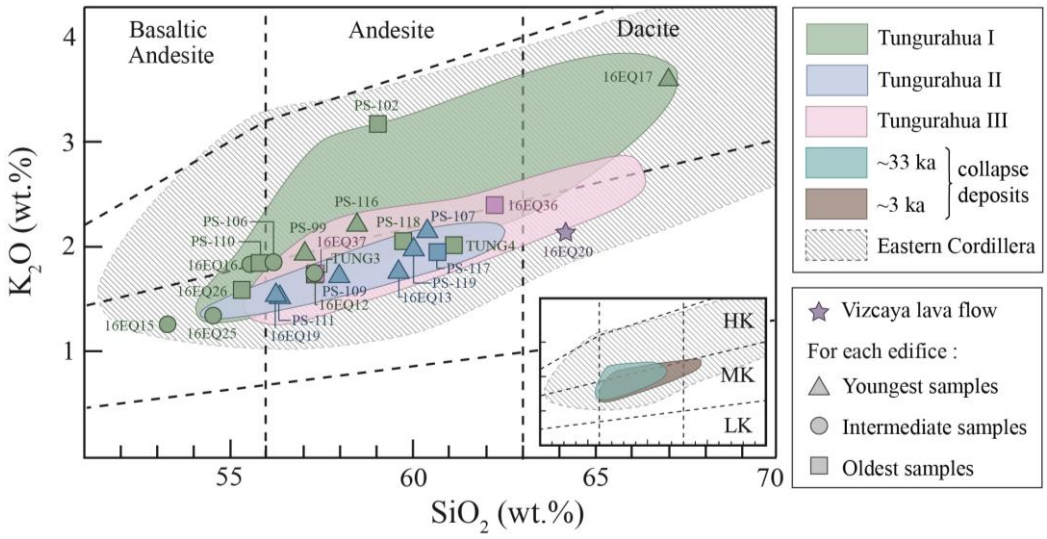

Fig. 7:

Variation diagrams showing the evolution of major elements (in wt. %) as a function of Th (in ppm). Symbols are the same used in Fig. 6. Coloured fields have been obtained from data published in Schiano et al. (2010) and analyses given in Appendix B. Samples from the latter have been associated to a unit considering their location and stratigraphical position.

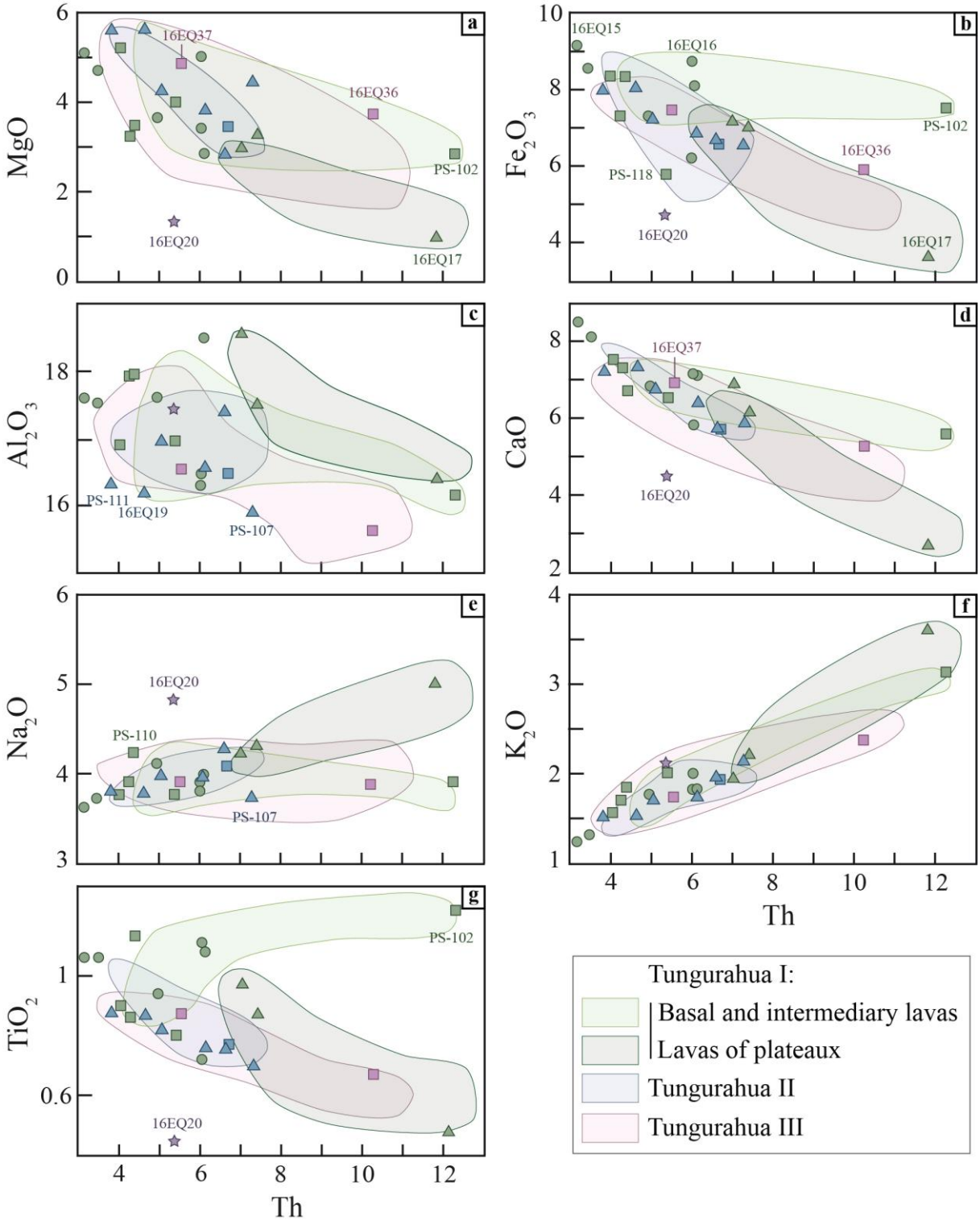

Fig. 8:

a) Incompatible elements normalized to primitive mantle spider diagram (Sun and McDonough, 1989). Hatched grey domain represent Eastern Cordillera data. Analysed samples are represented in green (Tungurahua I), blue (Tungurahua II), pink (Tungurahua III) and purple (Vizcaya lava flow). b) Rare Earth Elements normalized to chondrites diagram (Sun and McDonough, 1989). Symbols are the same used in Fig. 8a.

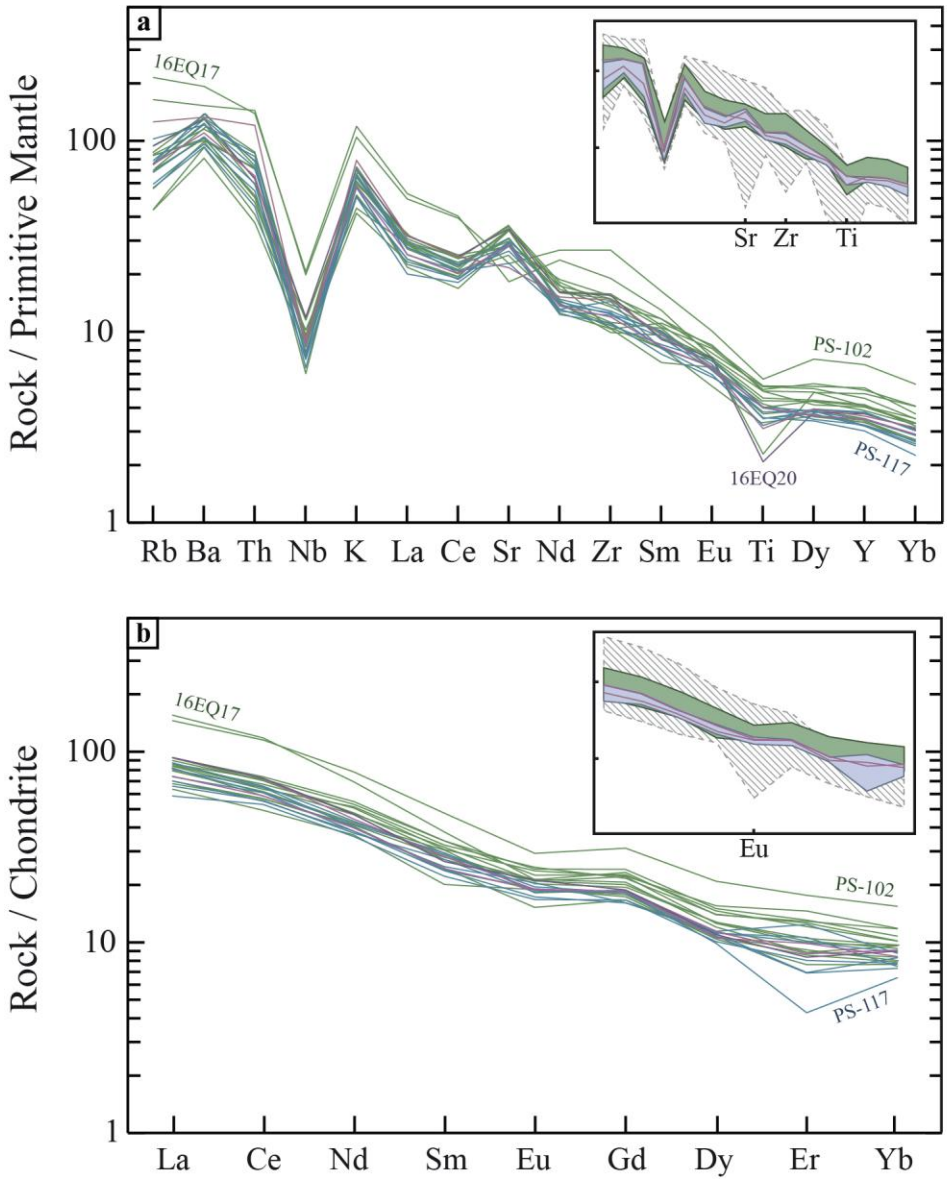

Fig. 9:

Variation diagrams of trace elements (in ppm). a-b) Sr and V vs. Th. c-d) (Sr/Y) and (La/Yb) vs. Th. e-f) (Sr/Y) vs. Y and (La/Yb) vs. Yb. "Adakite" and classical arc lavas fields from Castillo et al. (1999). Symbols, caption and references are the same used in Fig. 7.

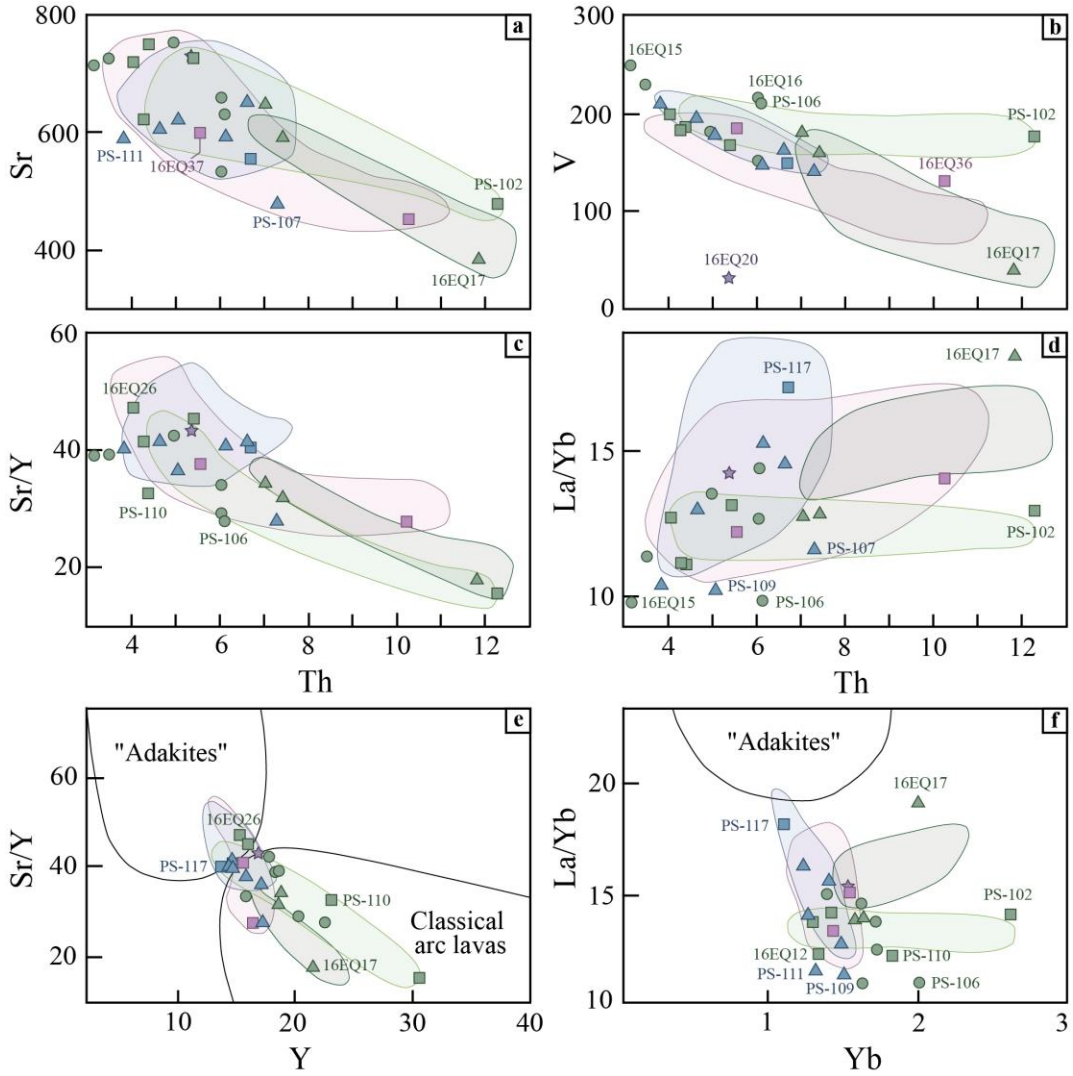

Fig. 10:

Morphological reconstruction of Tungurahua volcano: a) before the onset of activity, b) at the end of Tungurahua I construction, c) after the quiescent period preceding the first flank collapse (note that the western flank no longer crops out today, this is therefore a modelling based on the volumes of the deposits, and does not consider incised valleys), d) after the first western sector collapse, e) at the end of Tungurahua II construction, f),

after the collapse of the summit of Tungurahua II, and g) the current morphology, with the construction of Tungurahua III.

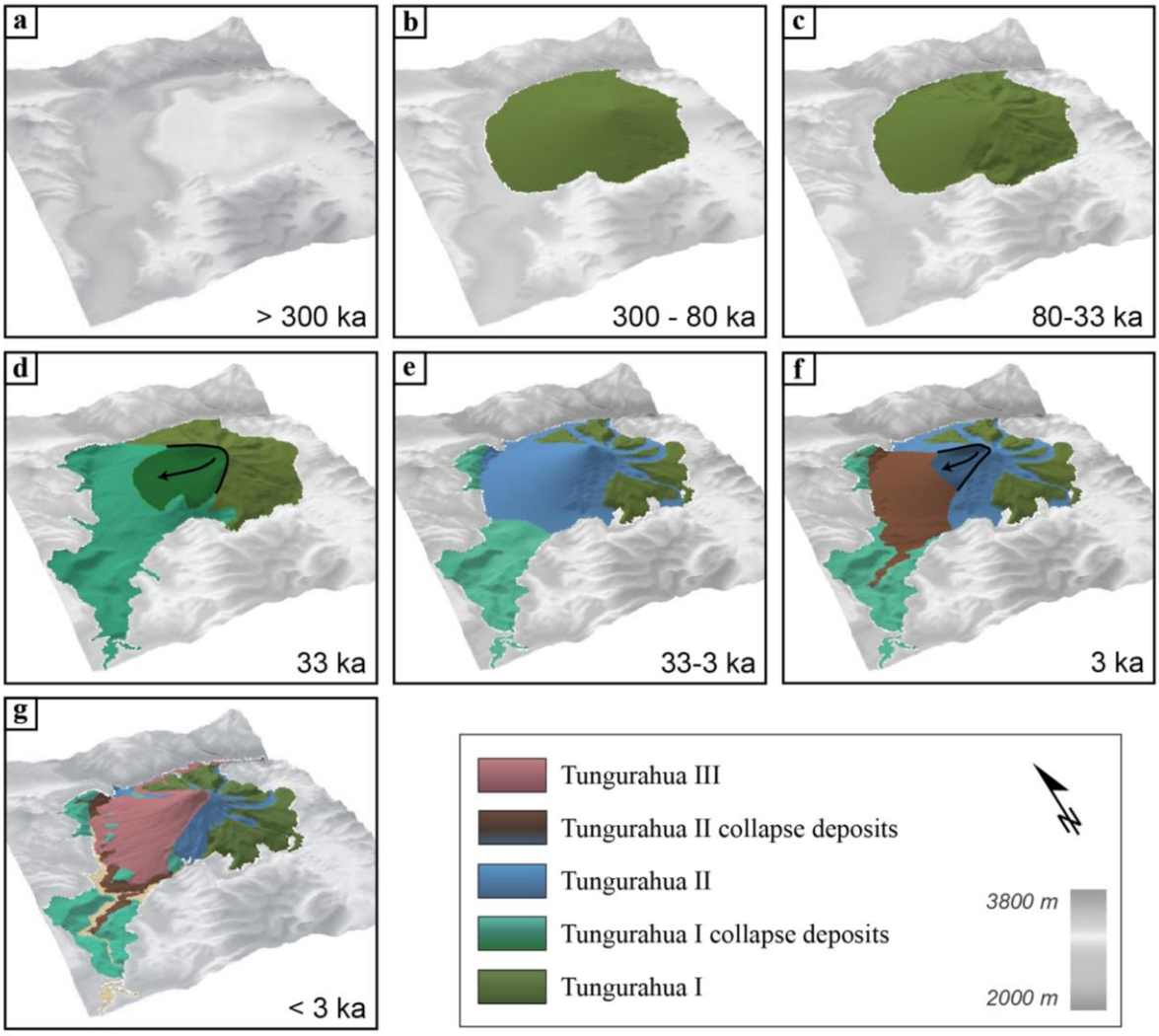

Fig. 11:

a) Overview of the "diamond-shape" plateau, located between Pondoa and Tungurahua III deposits. b) Cross-sectional view of the plateau, composed of Tungurahua I collapse deposits overlaid by Tungurahua II lava flows. c) Detailed view of Tungurahua I collapse deposits, showing blocks in a light breccia matrix. Most

massive blocks are highlighted by black dotted lines. d) 3-D view of the southwestern flank. Green line: ~33 ka collapse scar; blue line: ~3 ka collapse scar. Dotted lines delimit the three edifices.

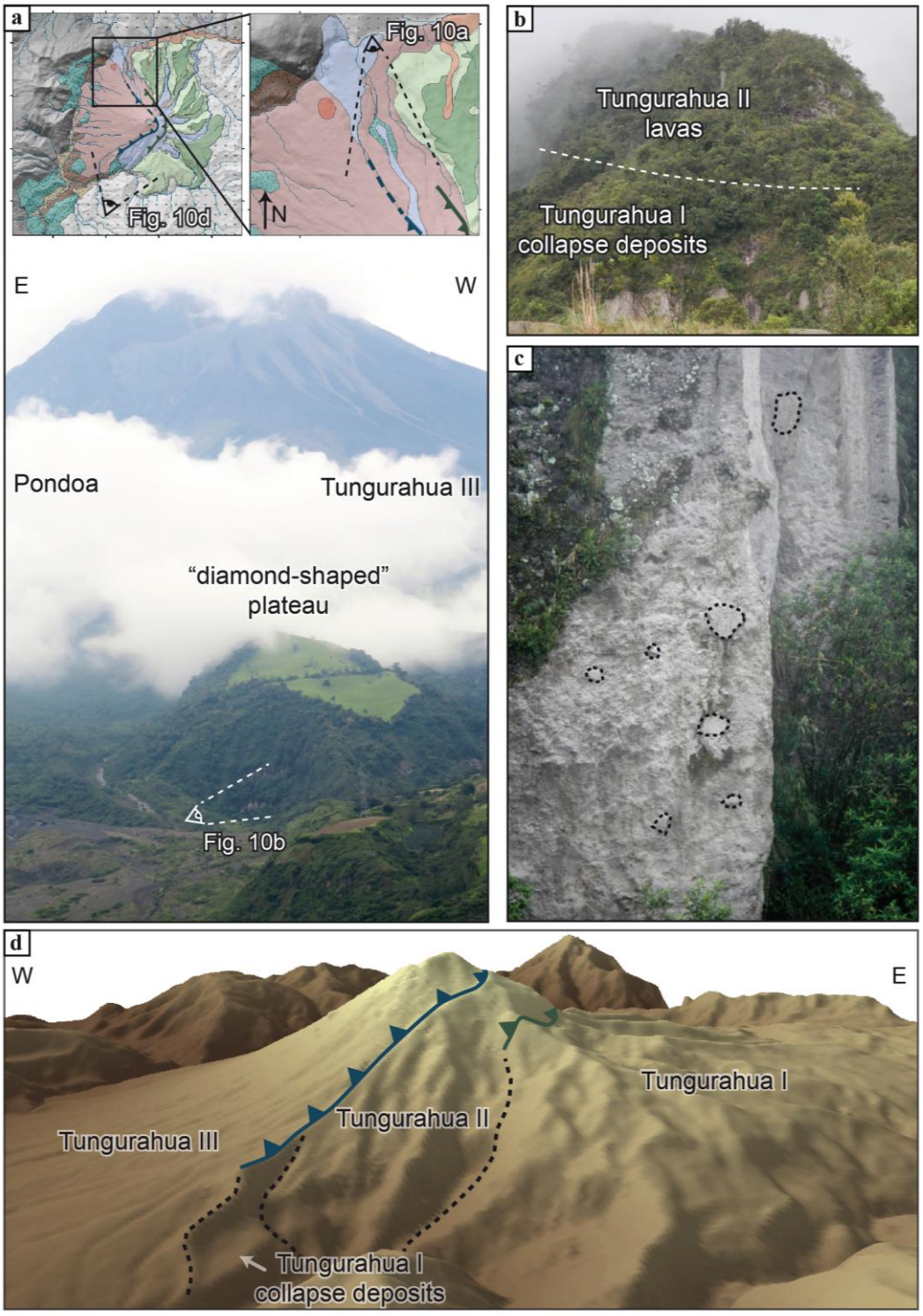

Fig. 12:

a) Mg# (=100*Mg/(Mg+Fe^{2+})) and SiO_2 (in wt. %) content as a function of chronology. b) La/Yb, La/Sm and Sm/Yb ratios as a function of chronology. Red dotted lines indicate the two sector collapses. Symbols are the

same used in Fig. 6. Coloured fields represent the range of Mg#, SiO_2 and REE ratios obtained from our non-dated samples and analyses given in Appendix B.

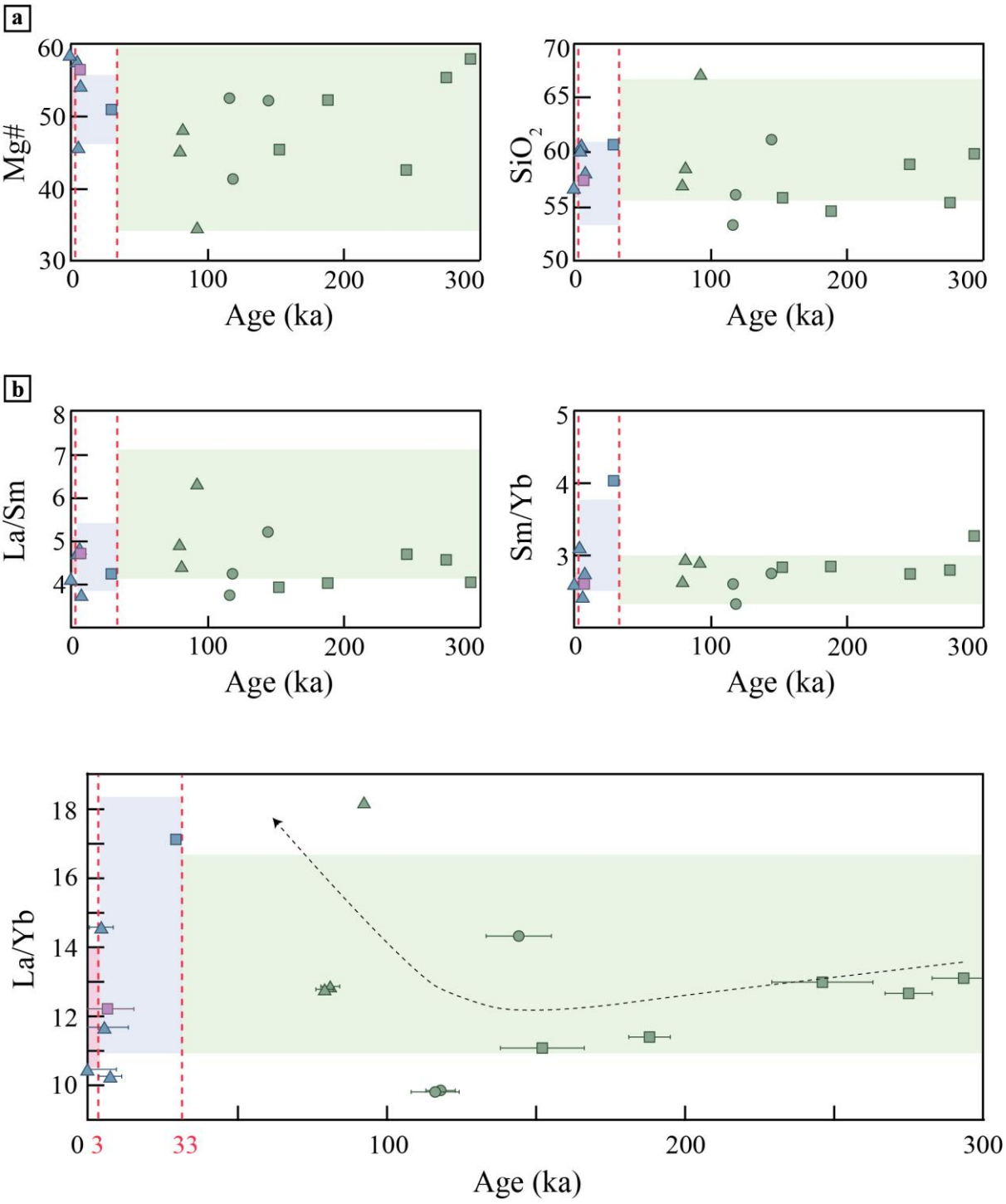

Table captions

Table 1:

New K-Ar ages obtained on groundmass in this study. Results are listed from the oldest to the youngest. Column headings indicate sample name, detail of the outcrop location, sample coordinates projected using the Universal Transverse Mercator (UTM) coordinate system (Zone 17), potassium concentration in percent, radiogenic argon content in percent and 10^{11} atoms per gram, ages and weighted mean age in ka, with 1-sigma accuracy. Ages marked with an asterisk (*) were calculated using unweighted average.

Table 2:

Major and trace element composition of whole-rock samples. All major data were brought down to a total of 100%. Samples marked with an asterisk (*) have not been dated.

Table 3:

Results of volumes, magmatic productivity and erosion rates calculations, given at 1-sigma accuracy, obtained from the palaeosurfaces modelling. Raw volume corresponds to the volume calculated from the surface model without taking into account erosion that occurred during the construction. Total volume corresponds to the sum of the raw volume and the volume eroded during the construction, based on the erosion rate. Min-max values were calculated by dividing the minimum volume by the maximum time period, and the maximum volume by the maximum time period, respectively. Erosion rate in T/km2/ka was calculated considering a rock mean density of 2.7. Ages marked with an asterisk (*) are previous 14C published ages (Le Pennec et al., 2013).

Table 4:

Summary of Tungurahua eruptive and erosion rates, compared to rates from other published studies.

Appendix captions

Appendix A:

Thin sections of all samples (in alphabetical order), observed under an optical microscope. Photographs in left-hand column were taken with a polarized light, and in right-hand column with a natural light.

Appendix B:

Major and trace element composition of Tungurahua whole-rock samples, presented in Hall et al. (1999) and in Bustillos (2008). All major data were brought down to a total of 100%. Column headings indicate edifice, sample name, outcrop coordinates projected using the Universal Transverse Mercator (UTM) coordinate system (Zone 17) and given within 100 meters, and volcanic unit. Results are listed in two parts: lavas, from potentially oldest to youngest, then blocks belonging to sector collapse deposits. pl : plateau.

Appendix C:

KMZ file containing the location of the samples described in this article.